

1  
2  
3  
4  
5  
6  
7  
8  
9  
10  
11  
12

# A Linear Response Framework for Radiative-Convective Instability

Tom Beucler<sup>1</sup>, Timothy Cronin<sup>1</sup>, Kerry Emanuel<sup>1</sup>

<sup>1</sup>Lorenz Center, Department of Earth Atmospheric and Planetary Sciences, Massachusetts Institute of Technology, Cambridge, MA 02139, USA.

## Key Points:

- We combine linear responses of diabatic heating with the weak temperature gradient approximation to analyze radiative-convective instability
- The stability of radiative-convective equilibrium to moisture perturbations depends on how heating is converted into vertical moisture advection
- Although clear-sky radiative heating is potentially destabilizing, the convective response to moisture dominates the linear stability problem

---

Corresponding author: Tom Beucler, [tom.beucler@gmail.com](mailto:tom.beucler@gmail.com)

**Abstract**

Radiative-convective equilibrium (RCE) is a simple paradigm for the tropical climate, in which radiative cooling balances convective heating in the absence of lateral energy transport. Recent studies have shown that a large-scale circulation may spontaneously develop from RCE through the interactions among water vapor, radiation, and convection. This potential instability, referred to as radiative-convective instability, may be posed as a linear stability problem for the water vapor profile by combining a linear response framework with the weak temperature gradient approximation. We design two analytic models of convective linear response to moisture perturbations, which are similar to Betts-Miller and bulk-plume convection schemes. We combine these convective responses with either clear-sky gray or real-gas radiative responses. In all cases, despite consistent radiative feedbacks, the characteristics of convection dominate the vertical structure of the most unstable linear mode of water vapor perturbations. For Betts-Miller convection, the stability critically depend on a key parameter: the heating to advection of moisture conversion rate (HAM); warmer atmospheres with higher HAM exhibit more linear instability. In contrast, bulk-plume convection is stable across temperatures, but becomes linearly unstable with a moisture mode peaking in the mid-troposphere once combined to radiation, with approximate growth rates of 10 days.

**1 Introduction**

Radiative-convective equilibrium (RCE) is the state of the atmosphere in which convective heating balances radiative cooling without lateral transport of moisture or energy [e.g., review by *Ramanathan and Coakley, 1978*]. Although RCE is a natural basic state for the tropical atmosphere, its stability to small water vapor perturbations remains poorly understood, because of the complexity of the interaction among atmospheric water vapor, clouds, radiation, and convection. Water vapor directly interacts with radiation by changing the local emissivity of the atmosphere and the vertical structure of atmospheric radiative cooling. Furthermore, water vapor indirectly interacts with radiation by influencing the formation of clouds. Both of these interactions have the potential to amplify water vapor perturbations: they have been found to be important for spontaneous cyclogenesis [e.g., *Wing et al., 2016*], and the self-aggregation of convection, through mechanism denial experiments [e.g., *Bretherton et al., 2005; Muller and Held, 2012; Holloway and Woolnough, 2016*] and energy budgets [e.g., *Wing and Emanuel, 2014; Wing and Cronin, 2016*]. These interactions depend on temperature [e.g., *Emanuel et al., 2014; Beucler and Cronin, 2016*], clouds, and the structure of the moisture perturbation [e.g., *Beucler and Cronin, 2016*], making them inseparable from atmospheric convection. The interaction between water vapor and convection has been studied in the contexts of the Madden-Julian oscillation [e.g., *Hannah and Maloney, 2011; Grabowski and Moncrieff, 2004*] and the self-aggregation of convection in convection-permitting models [e.g., *Muller and Bony, 2015; Tompkins, 2001*]. The unstable nature of this interaction has been referred to as the moisture-convection feedback, and its physics remain unclear. This feedback could rely on updrafts being less cooled by entrainment in a moist environment [e.g., *Tompkins, 2001; Mapes and Neale, 2011; Holloway and Neelin, 2009*], or on an anomalously moist boundary layer favoring convection by increasing local buoyancy [e.g., *Wing et al., 2017*]. Because these interactions have been diagnosed from non-linear numerical models, their physical mechanisms are intertwined and hard to interpret, motivating the question:

What physical mechanisms govern the interactions between water vapor and convection, and between water vapor and radiation, and how do these interactions affect the evolution of a water vapor perturbation?

In this paper, we use a bottom-up approach to diagnose the physics of the interactions among water vapor, radiation, and convection, near a basic state of RCE. To keep the problem tractable, we neglect cloud-radiation interactions and focus on clear-sky radiation. By examining the effect of a water vapor perturbation on both atmospheric convection and ra-

60 **Figure 1.** The interaction of a water vapor perturbation with atmospheric radiation and convection leads to  
 61 a water vapor tendency that can amplify, damp, or move the perturbation.

66 diation, we predict how a water vapor perturbation would evolve over a time scale of  $\sim 10$   
 67 days (Figure 1). We adopt a linear response approach to quantitatively evaluate the separate  
 68 contributions from convective heating and moistening, as well as from longwave and short-  
 69 wave radiative heating. We parametrize large-scale dynamics by using the weak temperature  
 70 gradient (WTG) framework [e.g., *Sobel et al.*, 2001], where temperatures are fixed and the  
 71 net residual heating from convection and radiation drives large-scale vertical motions. Each  
 72 section of this paper addresses a separate question:

73 (Section 2) How can the water vapor tendency profile be computed from the water vapor  
 74 perturbation profile in the weak temperature gradient framework?

75 (Section 3) How does atmospheric convection linearly respond to water vapor pertur-  
 76 bations?

77 (Section 4) How does atmospheric radiation linearly respond to water vapor perturba-  
 78 tions?

79 (Section 5) How do small water vapor perturbations evolve as a consequence of their  
 80 influences on atmospheric radiation and convection?

81 Sections 3 to 5 can be read independently, and cross-references are included when nec-  
 82 essary.

## 83 2 Linear response framework

### 84 2.1 Linear response function

85 This section aims to relate the evolution of a small water vapor perturbation to its ef-  
 86 fects on radiative and convective diabatic tendencies. For that purpose, we consider a non-  
 87 rotating atmospheric domain that is large enough (e.g. 100km in the Tropics) to include both  
 88 a small cloudy area with deep convective ascent [typically a few percent of the total domain,  
 89 e.g., *Malkus et al.*, 1961; *Bjerknes*, 1938], and a large clear area with slow subsidence.

90 Following *Arakawa and Schubert* [1974]; *Yanai et al.* [1973], we assume that the do-  
 91 main’s dry static energy  $s$  [defined as the sum of the sensible heat and the potential energy,  
 92 e.g., *Yanai et al.*, 1973] and specific humidity  $q$  can both be approximated by their clear-sky  
 93 values. Furthermore, the domain is assumed to be much smaller than the Rossby radius of  
 94 deformation and the timescale much longer (e.g. 1 day) than the gravity wave adjustment  
 95 timescale, so that the weak temperature gradient approximation holds in the free troposphere.  
 96 Examples of strict WTG in the literature include the neglect of the free-tropospheric temper-  
 97 ature tendency in section 4 of *Sobel et al.* [2000] or below equation 2 of *Sobel et al.* [2003],  
 98 and the neglect of  $\Delta T$  except for the radiative perturbation in equation A4d of *Adames and*  
 99 *Kim* [2016]. Here, the strict version of the WTG approximation allows us to neglect the local  
 100 tendency of dry static energy ( $\partial s / \partial t = 0$ , where  $t$  represents time). The domain-averaged  
 101 free-tropospheric budgets of dry static energy and specific humidity are then given by:

$$\begin{aligned} \omega \frac{\partial s}{\partial p} &= g \left( \frac{\partial \mathcal{F}_{\text{DSE}}}{\partial p} + \frac{\partial \mathcal{F}_{\text{LW}}}{\partial p} + \frac{\partial \mathcal{F}_{\text{SW}}}{\partial p} \right), \\ \frac{\partial q}{\partial t} + \vec{u} \cdot \vec{\nabla} q + \omega \frac{\partial q}{\partial p} &= \frac{g}{L_v} \frac{\partial \mathcal{F}_{\text{LH}}}{\partial p}, \end{aligned} \quad (1)$$

102 where  $\vec{u}$  is the large-scale horizontal velocity,  $\vec{\nabla}$  the horizontal gradient operator,  $\omega$  the  
 103 large-scale vertical velocity (in units of  $\text{Pa s}^{-1}$ ), defined as the area-weighted average of the  
 104 ascending motion in the cloudy zone and the subsidence motion in the clear-sky zone,  $p$  the  
 105 atmospheric pressure and  $g$  is the gravitational acceleration.  $\mathcal{F}_{\text{DSE}}$  is the convective dry static

106 energy flux,  $\mathcal{F}_{\text{LW}}$  the net longwave flux,  $\mathcal{F}_{\text{SW}}$  the net shortwave flux, and  $\mathcal{F}_{\text{LH}}$  the convective  
 107 latent heat flux, all defined in units of  $\text{W m}^{-2}$ . The evaporation and condensation rates of  
 108 hydrometeors are included in the convective heating and moistening tendencies.  $L_v$  is the la-  
 109 tent heat of vaporization of water vapor, and we neglect the latent heat of fusion. Radiative-  
 110 convective equilibrium (RCE) is defined as the the statistically steady state of the previous  
 111 equations ( $\partial/\partial t = 0$ ), with no large vertical velocity ( $\vec{\nabla}, \omega = (\vec{0}, 0)$ ). From now on, we  
 112 denote deviations from RCE with primes ( $X'$ ), while unprimed variables ( $X$ ) denote RCE.  
 113 We linearize the previous equation about the basic state, RCE, by assuming that the devia-  
 114 tions  $X'$  are small compared to the basic-state statistical mean  $\bar{X}$ . Assuming that the WTG  
 115 approximation strictly holds for deviations from RCE, the linearized version of equations 1  
 116 is:

$$\begin{aligned} \omega' \frac{\partial s}{\partial p} &= g \left( \frac{\partial \mathcal{F}'_{\text{DSE}}}{\partial p} + \frac{\partial \mathcal{F}'_{\text{LW}}}{\partial p} + \frac{\partial \mathcal{F}'_{\text{SW}}}{\partial p} \right), \\ \frac{\partial q'}{\partial t} + \omega' \frac{\partial q}{\partial p} &= \frac{g}{L_v} \frac{\partial \mathcal{F}'_{\text{LH}}}{\partial p}. \end{aligned} \quad (2)$$

117 Combining the two previous equations in order to eliminate  $\omega'$  relates the evolution of the  
 118 perturbation specific humidity to the perturbation fluxes:

$$\underbrace{\frac{\partial q'}{\partial t}}_{\text{Moisture tendency}} = \frac{g}{L_v} \left[ \underbrace{\frac{\partial \mathcal{F}'_{\text{LH}}}{\partial p}}_{\text{Convective moistening}} + \alpha \left( \underbrace{\frac{\partial \mathcal{F}'_{\text{DSE}}}{\partial p}}_{\text{Convective heating}} + \underbrace{\frac{\partial \mathcal{F}'_{\text{LW}}}{\partial p}}_{\text{Longwave heating}} + \underbrace{\frac{\partial \mathcal{F}'_{\text{SW}}}{\partial p}}_{\text{Shortwave heating}} \right) \right], \quad (3)$$

119 where we have introduced the non-dimensional parameter  $\alpha$  that relates heating sources to  
 120 vertical advection of water vapor:

$$\alpha \stackrel{\text{def}}{=} -\frac{L_v \partial q / \partial p}{\partial s / \partial p} > 0. \quad (4)$$

121 This parameter has been previously introduced by *Chikira* [2014], studied in the context of  
 122 the Madden-Julien oscillation moisture-convective feedback in *Wolding et al.* [2016], and  
 123 corresponds to the ratio  $-M_q/M_s$  in equations 1 and 2 of *Sobel et al.* [2003]. From now  
 124 on, we refer to  $\alpha$  as the heating-to-advection-of-moisture (HAM) conversion factor (it is  
 125 positive-definite so long as dry static energy increases with height and specific humidity de-  
 126 creases with height). HAM is essentially an exchange rate between the heating rate and the  
 127 latent heat tendency in WTG; a value greater than 1 indicates that  $1 \text{ W kg}^{-1}$  of heating will  
 128 translate into more than  $1 \text{ W kg}^{-1}$  of latent heat tendency due to vertical advection by WTG-  
 129 derived vertical motion. Since  $\alpha \stackrel{\text{def}}{=} 1 - (\partial \text{MSE} / \partial p) (\partial s / \partial p)^{-1}$ , where  $\text{MSE} \stackrel{\text{def}}{=} s + L_v q$  is  
 130 the moist static energy, a decrease of moist static energy with height implies  $\alpha > 1$ , whereas  
 131 an increase of moist static energy with height implies  $\alpha < 1$ . Tropical profiles of moist static  
 132 energy generally have a "C" shape of moist static energy with a mid-tropospheric minimum;  
 133  $\alpha > 1$  below this minimum and  $\alpha < 1$  above it.  $1 - \alpha$  is closely related to the local defi-  
 134 nition of normalized gross moist stability (see equation 2 of *Kuang* [2012]), which usually  
 135 corresponds to convective amplification when negative through the net import of moisture  
 136 in the lower troposphere. Finally, although we will assume a base RCE state for the rest of  
 137 this study, this framework could be generalized to a base state with mean velocity ( $\vec{u}, \bar{\omega}$ ) by  
 138 adding  $\vec{u} \cdot \vec{\nabla} q + \bar{\omega} \partial q / \partial p$  on the left-hand side of the moisture equation 1,  $\vec{u} \cdot \vec{\nabla} q' + \bar{\omega} \partial q' / \partial p$   
 139 on the left-hand side of the moisture equation 2, and  $-\vec{u} \cdot \vec{\nabla} q' - \bar{\omega} \partial q' / \partial p$  on the right-hand  
 140 side of equation 3.

141 In summary, equation 3 states that under the WTG approximation, specific humidity  
 142 is changed directly by the local perturbation convective moistening, and also by the local  
 143 perturbation convective, longwave and shortwave heating rates through the effect they have  
 144 on the large-scale vertical velocity. Furthermore, equation 3 gives a framework to study the

145 linear instability of water vapor perturbations. RCE is an equilibrium state, meaning that the  
 146 right-hand side of equation 3 is zero in RCE. Therefore, the behavior of small water vapor  
 147 perturbations is determined by the value of the Jacobian in RCE [as long as it does not have  
 148 eigenvalues with zero real parts, e.g., *Hartman, 1960*]:

$$\frac{\partial}{\partial q'} \left[ \frac{\partial q'}{\partial t} \right]_{\text{RCE}} = \frac{g}{L_v} \left[ \frac{\partial^2 \mathcal{F}_{\text{LH}}}{\partial p \partial q'} + \alpha \left( \frac{\partial^2 \mathcal{F}_{\text{DSE}}}{\partial p \partial q'} + \frac{\partial^2 \mathcal{F}_{\text{LW}}}{\partial p \partial q'} + \frac{\partial^2 \mathcal{F}_{\text{SW}}}{\partial p \partial q'} \right) \right]_{\text{RCE}}, \quad (5)$$

149 where the subscript RCE means that the bracketed quantities are evaluated in radiative-convective  
 150 equilibrium, in which  $q' = 0$  by definition. Equation 5 is the WTG continuous version of  
 151 equations (7) and (25) of [*Emanuel et al., 2014*], respectively valid for a finite number of lay-  
 152 ers and two layers. If the Jacobian has at least one eigenvalue with positive real part, RCE  
 153 may be unstable to small water vapor perturbations. In models and observations, we work on  
 154 discrete pressure levels, motivating the introduction of the discrete counterpart to the Jaco-  
 155 bian: the linear response matrix.

## 156 2.2 Linear response matrix

157 We start by defining discrete levels of the atmosphere:  $i = 1, 2, \dots, N$ . For short time  
 158 periods following a small water vapor perturbation, we expect the atmosphere to respond  
 159 linearly, and the discrete version of equation 5 is:

$$\frac{dq'_i}{dt} = \sum_{j=1}^N M_{ij} \cdot q'_j, \quad (6)$$

160 where  $q'_j$  is the specific humidity perturbation at a level  $j$ ,  $dq'_i/dt$  the specific humidity ten-  
 161 dency in response to that perturbation at a level  $i$ , and  $M$  the linear response matrix in units  
 162  $s^{-1}$ , defined as the discrete counterpart of the continuous Jacobian. The linear response func-  
 163 tion approach has been used by *Kuang [2010]* to study convectively-coupled waves, and also  
 164 by *Herman and Kuang [2013]* to study the moistening and heating responses of several con-  
 165 vective parameterizations. Here, the atmospheric temperature profile is fixed, making the  
 166 linear response function a single two-dimensional matrix rather than a set of four matrices as  
 167 in the work by *Kuang [2010, 2012]*. The interpretation of our single linear response matrix is  
 168 described in Figure 2. In a model with equally-spaced pressure levels, the column-integrated  
 169 growth rate of a localized perturbation at level  $p_j$ ,  $\widehat{M}_j$  (in  $s^{-1}$ ) may be directly computed  
 170 from the linear response matrix:

$$\widehat{M}_j = \sum_{i=1}^N M_{ij}. \quad (7)$$

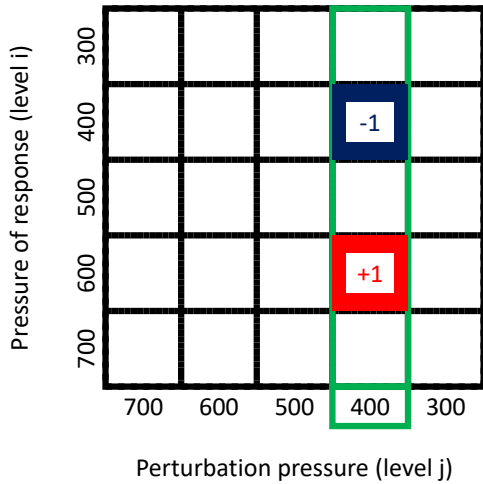
178 Using this matrix, we can predict the evolution of the structure and magnitude of a  
 179 small water vapor perturbation  $q'_i(t)$  as:

$$q'_i(t) = (\exp Mt)_{ij} \cdot q'_j(t=0) \quad (8)$$

180 for small times, where we have exponentiated the linear response matrix:

$$\exp Mt \stackrel{\text{def}}{=} \sum_{n=0}^{\infty} \frac{(Mt)^n}{n!}.$$

181 If  $M$  has at least one eigenvalue with positive real part, RCE may be unstable to a small ini-  
 182 tial perturbation  $q'_j(t=0)$ . From equation 6, we see that equal moist and dry perturbations  
 183 yield opposite responses, which is a consequence of using a linear framework. Therefore, an  
 184 atmospheric model should produce symmetric responses to opposite-signed perturbations if  
 185 it is working in its linear range, which allows testing of the linear assumption [(e.g., appendix  
 186 B1 of *Herman and Kuang, 2013*]. In order to gain more insight into the interactions among  
 187 water vapor, radiation, and convection, we decompose  $M$  into four components by writing

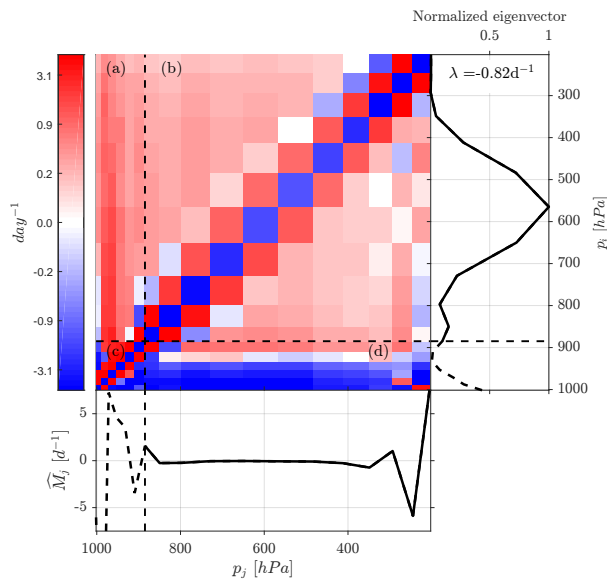


171 **Figure 2.** Guide to reading the linear response matrix  $M$ : The horizontal axis is the pressure at which  
 172 water vapor is perturbed ( $p_j$ , in hPa), while the vertical axis is the pressure of the water vapor response ( $p_i$ , in  
 173 hPa). In the example depicted above, water vapor is perturbed at  $p_j = 400$  hPa, and the water vapor tendency  
 174 response can be read in the green column. At the local perturbation level  $p_i = 400$  hPa, a negative matrix  
 175 element indicates that a perturbation would decay in time; below the perturbation level at  $p_i = 600$  hPa, a  
 176 positive matrix element indicates that a perturbation would amplify in time. In this simple case, a water vapor  
 177 perturbation at 400 hPa would be moved to 600 hPa at a unit rate.

188 the discrete counterpart of equation 5:

$$\underbrace{M}_{\text{Linear response}} = \underbrace{M_{\text{LH}} + M_{\text{DSE}}}_{\text{Convective response}} + \underbrace{M_{\text{LW}} + M_{\text{SW}}}_{\text{Radiative response}}, \quad (9)$$

189 where  $M_{\text{LH}}$  is the convective moistening response,  $M_{\text{DSE}}$  the convective heating response,  
 190  $M_{\text{LW}}$  the longwave heating response and  $M_{\text{SW}}$  the shortwave heating response. We have in-  
 191 corporated the evaporation and condensation of hydrometeors in the convective response,  
 192 which is valid as long as the perturbations are small enough not to saturate the domain at  
 193 any level. Because the atmosphere is assumed to be close to RCE, there is no advective re-  
 194 sponse on the right-hand side of equation 9. In RCE, gross moist stability [see *Yu et al.*,  
 195 1998; *Inoue and Back*, 2015] is undefined, as there is no horizontal flow ( $\vec{u} = 0$ ). However,  
 196 once the system is perturbed, gross moist stability is internally determined by the vertical  
 197 structure of the perturbation. If this internally-determined gross moist stability is negative, a  
 198 column-integrated moist static energy perturbation may grow spontaneously, potentially indi-  
 199 cating an unstable moisture-convection feedback. Some such scenarios of unstable moisture-  
 200 convection feedback would be unphysical, if they occurred from a basic state with zero moist  
 201 available potential energy. This could happen because of limitations of both the strict WTG  
 202 approximation and convective parameterizations, neither of which necessarily enforces the  
 203 physical requirement that circulations develop due to conversion of available potential en-  
 204 ergy to kinetic energy. The definition of moist available potential energy [e.g., *Stansifer et*  
 205 *al.*, 2017] is subtle, however, and further consideration of such possible unphysical moisture-  
 206 convection instabilities is left as a subject for future work. We will now proceed to compute  
 207 the linear response matrix in idealized and numerical models of convection and radiation.



218 **Figure 3.** Linear convective matrix from the linear response matrices of *Kuang* [2012], where the HAM has  
 219 been evaluated from the mean state of the simulation. The top of the boundary layer, identified as the relative  
 220 humidity maximum in the lower troposphere, is indicated with dashed black lines. (Bottom panel) Vertically-  
 221 integrated growth rate ( $\widehat{M}_j$  in  $\text{day}^{-1}$ ). (Right panel) Eigenvector corresponding to the leading eigenvalue real  
 222 part  $\lambda$ , normalized to have a maximum of 1.

### 208 3 Linear response of convection

209 The goal of this section is to gain physical insight into the linear convective response,  
 210 defined as the sum of the convective moistening response  $M_{\text{LH}}$  and the convective heating  
 211 response  $M_{\text{DSE}}$ . For that purpose, we analyze realistic convective responses from cloud-  
 212 permitting simulations, before calculating analytic WTG linear convective responses based  
 213 on toy models of convection similar to two widely used convective schemes.

214

#### 215 3.1 Convection in cloud-permitting models

216

##### 217 3.1.1 Linear response matrix of a cloud-permitting model

223 We start by analyzing realistic linear response matrices derived from a cloud-permitting  
 224 model and provided by Zhiming Kuang following the methodology he described in *Kuang*  
 225 [2010]. The System for Atmospheric Modeling [SAM *Khairoutdinov et al.*, 2003] is run  
 226 to RCE in a  $128 \times 128 \text{ km}^2$  square domain with 2km horizontal resolution and 28 vertical  
 227 levels, as described in section 4 of *Kuang* [2012]. *Kuang* [2012] ran all simulations using  
 228 a surface temperature of 301.15K, and integrated the perturbed runs for as long as 10,000  
 229 days to minimize the noise level of the linear response matrices. We calculate the WTG con-  
 230 vective response matrix by adapting equation 3 to the convective responses of moisture to  
 231 moisture perturbations ( $dq/dt$  from  $q'$ ) (in  $\text{s}^{-1}$ ) and temperature to moisture perturbations

232  $(dT/dt$  from  $q'$ ) (in K/s per kg/kg) [respectively figures 8b and 8c from *Kuang, 2012*]:

$$\underbrace{M_{\text{LH}}}_{\text{Convective moistening}} = \left( \frac{dq}{dt} \text{ from } q' \right) \mid \underbrace{M_{\text{DSE}}}_{\text{Convective heating}} = \alpha \frac{c_p}{L_v} \left( \frac{dT}{dt} \text{ from } q' \right), \quad (10)$$

233 where  $c_p$  is the specific heat capacity of dry air at constant pressure and the HAM  $\alpha$  is cal-  
 234 culated from the mean thermodynamic profiles of the SAM RCE simulation of *Kuang* [2012].  
 235 The linear convective response, sum of the convective moistening and heating responses, is  
 236 depicted in figure 3. We subdivide the convective linear response into four regions:

- 237 • (a) The strong free-tropospheric convecting heating resulting from boundary-layer
- 238 moisture perturbations,
- 239 • (b) The free-tropospheric convective heating and moistening responses to free-tropospheric
- 240 moisture perturbations,
- 241 • (c) The local response to boundary-layer moisture perturbations (dominated by water
- 242 vapor mixing),
- 243 • (d) The cooling and drying of the boundary layer resulting from free-tropospheric
- 244 moisture perturbations.

245 Although combining convective heating and moistening responses into a single WTG re-  
 246 sponse is always mathematically possible, it does not directly inform us on the evolution of  
 247 water vapor perturbations in the boundary layer where WTG breaks down because of hor-  
 248 izontal buoyancy gradients (regions a,c,d). In this study, we focus on explaining the free-  
 249 tropospheric response to free-tropospheric perturbations (region b) and its consequences for  
 250 the linear stability of water vapor perturbations. It is possible to separate the convective re-  
 251 sponse into three separate components:

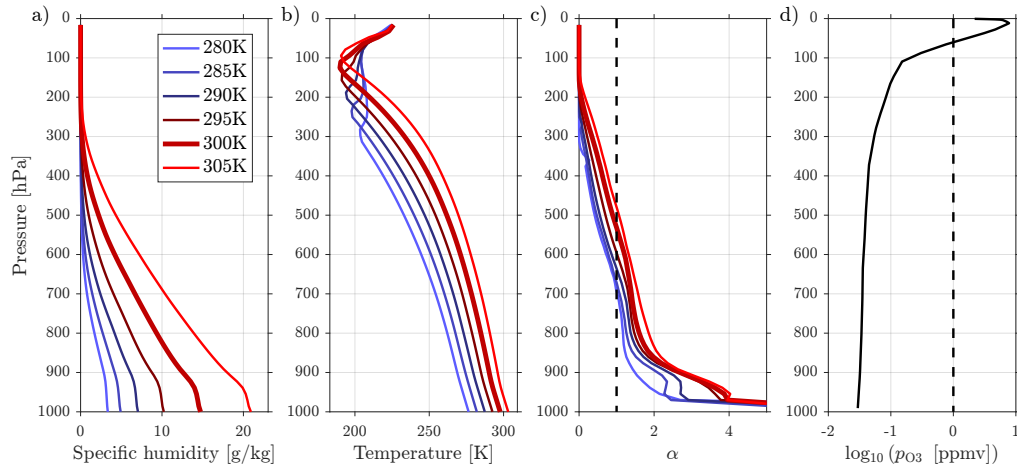
- 252 1. A local drying of moisture perturbations (blue diagonal), with strong local mixing of
- 253 water vapor (red squares right above and right below the blue diagonal),
- 254 2. A troposphericly-uniform convective heating, which decreases with height due to
- 255 the modulation by the HAM profile (red lower-right triangle and small part of the red
- 256 upper-left triangle),
- 257 3. A combination of convective heating and moistening above the diagonal (most of the
- 258 red upper-left triangle).

259 The combination of these three components leads to a stable convective response in RCE  
 260 (the leading real eigenvalue is  $-0.82\text{day}^{-1}$ ), consistent with the stability of RCE in *Kuang's*  
 261 cloud-permitting simulations. Constructing convective responses and combining them with  
 262 radiative responses for a variety of basic states is computationally expensive and difficult  
 263 to interpret in cloud-permitting simulations. Therefore, we proceed to the construction of  
 264 simple convective responses that mimic the two components of more realistic responses. Be-  
 265 fore doing so, we calculate different basic RCE states for our simple convective models from  
 266 cloud-permitting simulations.

267

### 268 **3.1.2 Radiative-convective equilibria from cloud-permitting simulations**

271 To provide basic states of temperature and specific humidity, we use simulations of  
 272 RCE conducted by Tristan Abbott on the Engaging computational cluster at MIT, using ver-  
 273 sion 6.10.6 of the SAM cloud-permitting model. The surface temperature varies from 280K  
 274 to 305K in increments of 5K between simulations. The horizontal domain is  $96 \times 96$  grid  
 275 cells with 1 km horizontal resolution, while the stretched vertical grid has 64 levels, with  
 276 eight levels below 1km and 500m vertical resolution above 3km. The upper boundary is a  
 277 rigid lid at 28km height, and a sponge layer from 19km to 28km prevents excessive gravity



269 **Figure 4.** Vertical profiles of (a) specific humidity (in g/kg), (b) temperature (in K), (c) HAM and (d) log  
 270 10 of the ozone volume concentration (in ppmv) in the SAM simulations ran by Tristan Abbott.

278 wave reflection off of the top of the model domain. Insolation is set to an equinoctial diurnal  
 279 cycle at 19.45 degrees North, producing a time-mean insolation of  $413.6\text{Wm}^{-2}$ . We use the  
 280 radiation code from the National Center for Atmospheric Research Community Atmosphere  
 281 Model version 3 *Collins et al.* [2006] and set the carbon dioxide mixing ratio to 355ppmv,  
 282 and the ozone mixing ratio to the standard tropical profile in SAM in all simulations. Micro-  
 283 physics are parameterized with the SAM single-moment microphysics scheme, documented  
 284 in *Khairoutdinov et al.* [2003]. No large-scale forcing of winds, temperature, or moisture is  
 285 imposed in any simulations. In these simulations, convection remains disaggregated (referred  
 286 to as “pop-corn” convection), and the thermodynamic profiles (shown in figure 4) are aver-  
 287 aged in space and time over 60 days after a 40 day spin-up. The column water vapor varies  
 288 from  $7.9\text{kg.m}^{-2}$  to  $68.7\text{kg.m}^{-2}$  from the coldest to warmest surface temperature (Figure 4a).  
 289 The temperature profile is close to a moist adiabatic profile in the lower troposphere and pro-  
 290 gressively approaches a dry adiabat near the tropopause (Figure 4b). Finally, the HAM pro-  
 291 file is very large in the boundary layer (with values up to 10 near the surface), decreases be-  
 292 low 1 in the lower to mid-troposphere before asymptoting to 0 near the tropopause (Figure  
 293 4c). Only the warmest surface temperature has a free-tropospheric-averaged  $\alpha$  larger than 1.  
 294 The reference simulation for sections 3 and 4 uses a surface temperature of 300K and is de-  
 295 noted with a thicker line in figure 4. Its column water vapor is  $44.5\text{kg.m}^{-2}$ , column relative  
 296 humidity 84%, tropopause pressure 121hPa, tropopause temperature 190K, and its HAM has  
 297 a mean free-tropospheric value of 0.91. The standard tropical ozone profile in SAM (Figure  
 298 4d) has a column ozone of  $5.3\text{g.m}^{-2}$ ; its mixing ratio reaches a minimum of 30ppbv at the  
 299 surface and a maximum of 7.8ppmv in the upper atmosphere.

### 300 3.1.3 Toy models of convective response

301 Starting from the 300K reference simulation, we construct Betts-Miller-like and bulk-  
 302 plume-like convective linear responses, with our schemes designed so that tendencies of wa-  
 303 ter vapor and temperature are zero in the reference state. The 2 toy models provide mean-  
 304 ingful linear responses about the same basic state under the WTG approximation, responses we  
 305 can then directly compare. For brevity, we refer to the 2 toy models as simply “Betts-Miller”  
 306 and “bulk-plume” schemes, keeping in mind that we have chosen toy models over their more  
 307 realistic counterparts and traded realism for analytical tractability. Since the eigenvalues of  
 308 radiative-convective instability are very sensitive to the convective response, this choice is a  
 309 first step that provides novel physical insight.

310

### 3.2 Betts-Miller scheme

311

#### 3.2.1 Description

312

313

314

315

316

317

318

319

The Betts-Miller convective scheme *Betts and Miller* [1986, 1993], commonly used as a minimal model of moist convection [e.g., *Frierson, 2007*], computes precipitation and convective tendencies based on the deviation of the temperature and water vapor profiles from reference values in a convectively unstable atmosphere. In the free troposphere, the scheme relaxes moisture and temperature perturbations to zero in time  $\tau_{\text{BM}}$ , where  $\tau_{\text{BM}}$  is a parameter of the scheme (typically a few hours). In order to conserve the moist static energy of the convecting layer, the scheme shifts the temperature profile in time  $\tau_{\text{BM}}$ , by a uniform amount  $(\Delta T)_{\text{BM}}$  given by:

$$(\Delta T)_{\text{BM}} = \frac{1}{c_p (p_b - p_t)} \int_{p_t}^{p_b} (c_p T_{\text{BM}} + L_v q_{\text{BM}}), \quad (11)$$

320

321

322

323

where  $c_p$  is the specific heat constant of dry air at constant pressure,  $L_v$  the latent heat of vaporization of water vapor,  $p_b$  the pressure at the top of the planetary boundary layer,  $p_t$  the tropopause pressure,  $T_{\text{BM}}$  the temperature perturbation from the Betts-Miller reference profile and  $q_{\text{BM}}$  the specific humidity perturbation from the Betts-Miller reference profile.

324

#### 3.2.2 Linear response

325

326

327

328

329

The theoretical framework of section 2 provides two simplifying constraints. First, we can linearize equation 11 about RCE and note that:  $(T'_{\text{BM}}, q'_{\text{BM}}) = (T', q')$ . Second, under the WTG approximation, the temperature perturbation  $T'$  is zero. Since the convective heating is given by the tendency of  $(\Delta T)_{\text{BM}}$ , its perturbation solely depends on the moisture perturbation  $q'$ .

330

331

332

333

334

335

336

337

338

In order to evaluate the linear response of the Betts-Miller scheme, we introduce a water vapor perturbation  $q'_j$  in a thin pressure layer  $[p_j - \Delta p/2, p_j + \Delta p/2]$ , for which the pressure thickness  $\Delta p$  is much smaller than the pressure level  $p_j$ . The pressure level  $p_j$  is above the top of the boundary layer, defined as the level of maximal relative humidity (928hPa for the reference profile), and below the tropopause, defined as the level of minimal temperature (188hPa for the reference profile). We assume that the whole atmosphere between these two levels is convecting. In response to the water vapor perturbation  $q'_j$ , the scheme relaxes  $q'_j$  to zero in time  $\tau_{\text{BM}}$ , corresponding to a local damping of the water vapor perturbation. Therefore, the convective moistening response matrix (in units  $s^{-1}$ ) is given by:

$$(M_{\text{LH}})_{ij} \stackrel{\text{def}}{=} \frac{1}{q'_j} \left( \frac{dq'_i}{dt} \right)_{\text{BM}} = \underbrace{-\frac{\delta_{ij}}{\tau_{\text{BM}}}}_{\text{Local drying}}, \quad (12)$$

339

340

341

342

343

where  $i$  is the response level,  $j$  the perturbation level, BM a subscript denoting the action of the Betts-Miller scheme and  $\delta_{ij}$  the Kronecker symbol, defined as 1 if  $i = j$  and 0 otherwise. In contrast, the convective heating in response to the perturbation moistening is equally distributed over all layers of the atmospheric column, corresponding to the following convective heating response:

$$(M_{\text{DSE}})_{ij} \stackrel{\text{def}}{=} \frac{\alpha_i}{L_v q'_j} \frac{c_p (\Delta T)'_{\text{BM}}}{\tau_{\text{BM}}} = \underbrace{\frac{\alpha_i}{\tau_{\text{BM}}} \frac{\Delta p}{p_b - p_t}}_{\text{Heating everywhere}}, \quad (13)$$

344

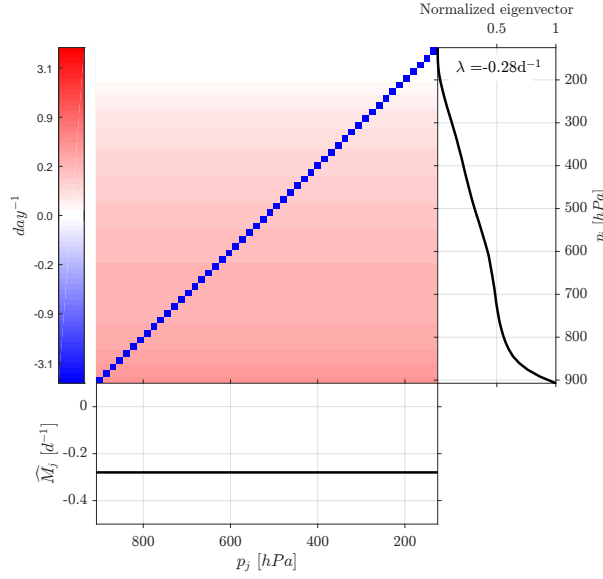
345

346

347

348

where  $M_{\text{DSE}}$  is the convective heating response matrix (in units  $s^{-1}$ ),  $\alpha_i$  the HAM (equation 4) evaluated at the response level  $p_i$ , and  $(p_b - p_t)$  the thickness of the free troposphere. Figure 5 represents the convective linear response of the Betts-Miller scheme with SAM RCE profiles as our basic state. Thus, the response of the Betts-Miller scheme to moist perturbations can be separated in two parts:



353 **Figure 5.** Betts-Miller linear convective matrix for  $\tau_{\text{BM}} = 3$  hours, where the HAM has been evaluated  
 354 from the reference SAM RCE profile. (Bottom panel) Vertically-integrated growth rate ( $\widehat{M}_j$  in  $\text{day}^{-1}$ ). (Right  
 355 panel) Eigenvector corresponding to the leading eigenvalue real part  $\lambda$ , normalized to have a maximum of 1.

- 349
- A local convective drying along the diagonal, where perturbations are removed in  
 350 time  $\tau_{\text{BM}}$ .
  - A tropospherically-uniform convective heating which has a growth rate that decreases  
 351 with height due to modulation by the HAM profile (equation 13).  
 352

### 356 3.3 Bulk plume equations

#### 357 3.3.1 Description

358 Most of the parameterizations that represent precipitating convection use bulk schemes,  
 359 which model an ensemble of different cumulus elements as a small number of entraining-  
 360 detraining plumes. *Plant* [2009] reviews the theoretical basis for different bulk parameteriza-  
 361 tions and spectral parameterizations (e.g. *Arakawa and Schubert* [1974]). Here, we start with  
 362 a simplified form of the bulk-plume equations for a single updraft plume developed by *Yanai*  
 363 *et al.* [1973], which has been used by *Romps* [2014] in order to estimate the moisture profile  
 364 from specified entrainment, detrainment, and mass flux profiles:

$$-g \frac{\partial m}{\partial p} = e - d, \quad (14)$$

$$-g \frac{\partial (mq^*)}{\partial p} = eq - dq^* - c, \quad (15)$$

$$-g \frac{\partial (mq)}{\partial p} = eq - dq^*, \quad (16)$$

$$-g \frac{\partial [m(s + L_v q^*)]}{\partial p} = e(s + L_v q) - d(s + L_v q^*), \quad (17)$$

368 where  $g$  is the gravitational acceleration,  $m$  is the cloud updraft mass flux (in units  $\text{kg}\cdot\text{m}^{-2}\cdot\text{s}^{-1}$ ),  
 369  $p$  is the hydrostatic pressure,  $(e, d, c)$  are the entrainment, detrainment and condensation rates  
 370 (in units  $\text{s}^{-1}$ ),  $q^*$  is the saturation specific humidity, and  $q$  is the environmental specific hu-  
 371 midity. To keep the model analytically tractable, we have neglected thermodynamical details  
 372 of the bulk plume model, including:

- 373 • The weight of the condensate on the right-hand side of the mass equation 14, which is  
 374 reasonable for small values of  $q^*$ .
- 375 • The evaporation of condensate on the right-hand side of the environmental moisture  
 376 equation 16, which assumes that any condensate instantly falls to the surface without  
 377 re-evaporating in the clear-sky environment. This is a poor approximation to reality,  
 378 as clear-sky re-evaporation balances the difference between convective heating and  
 379 radiative cooling in RCE.
- 380 • The difference between the dry static energy of the clouds and the environment [neu-  
 381 tral buoyancy assumption if virtual effects are ignored, e.g., *Singh and O’Gorman,*  
 382 2013], which affects the right-hand side of the moist static energy equation 17.
- 383 • The mixing between the neutral air of the troposphere and the stably stratified air of  
 384 the stratosphere, which can occur through convective overshooting and gravity wave  
 385 breaking.

### 386 3.3.2 Basic state

387 Assuming that the bulk-plume equations apply, we aim at diagnosing the equilibrium  
 388 updraft mass flux, detrainment, entrainment and condensation rates from RCE moisture  
 389 and temperature profiles. In appendix A.1, we show that the bulk-plume equations lead to  
 390 a unique set of solutions for the equilibrium convective profiles:

$$m(p) = \frac{\widehat{Q}_{\text{BP}} \cdot I(p)}{L_v q_{\text{def}}}, \quad (18)$$

$$e(p) = \frac{g \widehat{Q}_{\text{BP}} \cdot I(p)}{L_v^2 q_{\text{def}}^2} \frac{\partial (s + L_v q^*)}{\partial p}, \quad (19)$$

$$d(p) = \frac{g \widehat{Q}_{\text{BP}} \cdot I(p)}{L_v q_{\text{def}}^2} \frac{\partial q}{\partial p}, \quad (20)$$

$$c(p) = -\frac{g \widehat{Q}_{\text{BP}} \cdot I(p)}{L_v^2 q_{\text{def}}^2} \frac{\partial s}{\partial p}, \quad (21)$$

394 where  $\widehat{Q}_{\text{BP}}$  is the total free-tropospheric atmospheric cooling (a free parameter of our simple  
 395 bulk-plume model),  $p_b$  is the pressure at the top of the planetary boundary layer; we have  
 396 introduced the function  $I$ :

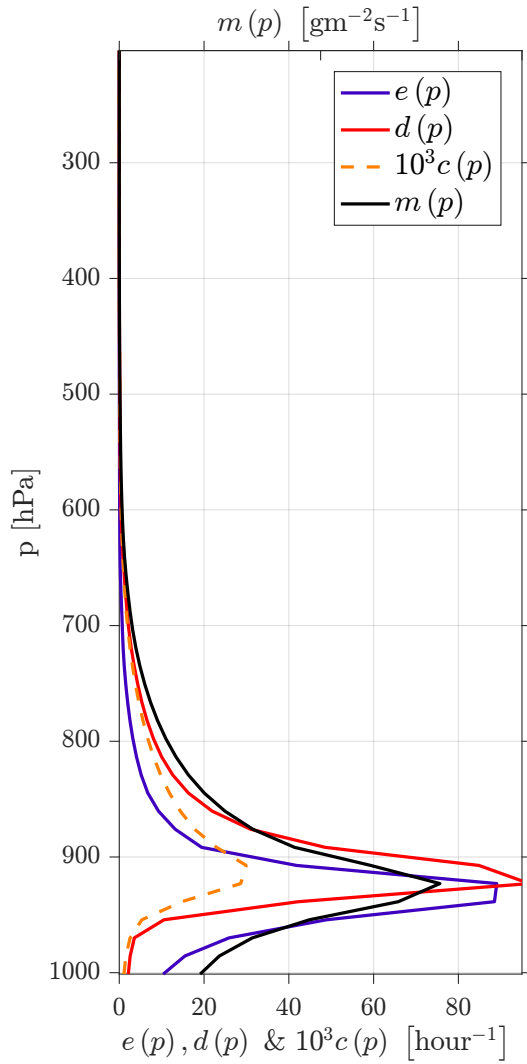
$$I(p) \stackrel{\text{def}}{=} \exp \left[ \int_{p_b}^p \frac{dp'}{L_v q_{\text{def}}(p')} \frac{\partial s(p')}{\partial p'} \right],$$

397 as well as the saturation deficit  $q_{\text{def}}$ :

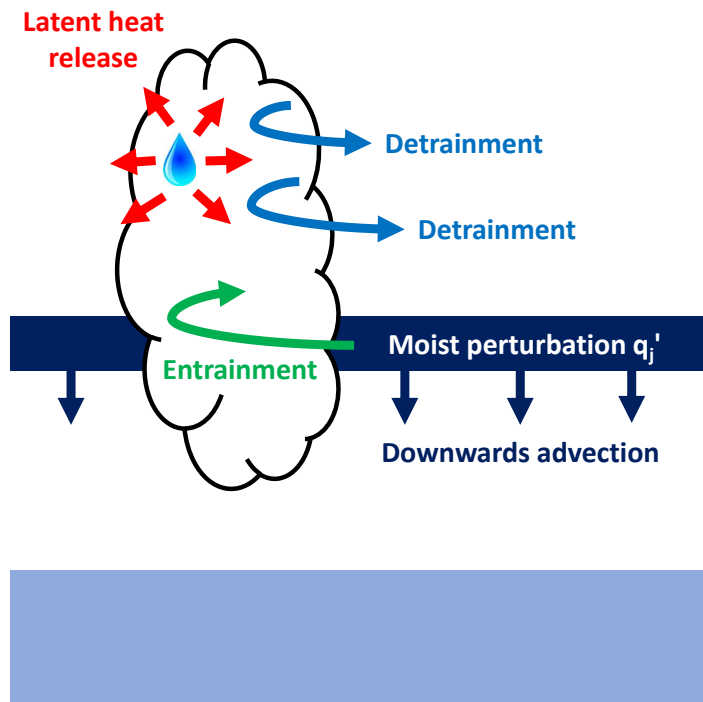
$$q_{\text{def}} \stackrel{\text{def}}{=} (q^* - q). \quad (22)$$

398 Taking the reference SAM RCE profiles as RCE leads to the convective profiles shown in  
 399 Figure 6.

402 Although our simple model captures the order-of-magnitude of convective prop-  
 403 erties overall [e.g., Figures 5 and 6 of *Pauluis and Mrowiec, 2013*], the entrainment rates  
 404 can artificially take negative values in the upper troposphere and at the top of the boundary  
 405 layer, where the saturated moist static energy decreases with height. This limitation of the



400 **Figure 6.** Entrainment and detrainment rate profiles (in  $\text{hour}^{-1}$ ) and condensation rate profile (in  $\text{month}^{-1}$ )  
 401 in RCE, as diagnosed from the reference SAM RCE temperature and moisture profiles.



413 **Figure 7.** The moist perturbation at level  $p_j$  is entrained in the cloudy updraft, where it detrainment and re-  
 414 leases latent heat through condensation at level  $p_{i>j}$  above the perturbed level. The moist perturbation is also  
 415 advected downwards to level  $p_{j-1}$  by the subsidence mass flux.

406 entrainment diagnostics remains if ice precipitation is taken into account [e.g., equation 22 of  
 407 *Pauluis and Mrowiec, 2013*] or if we take into account the weight of condensate and/or the  
 408 re-evaporation of condensates in the clear-sky environment (not shown). Taking into account  
 409 troposphere-stratosphere mixing, the preferential detrainment of plumes with low saturated  
 410 moist static energy, or cloud-top mixing would (at least partly) correct this issue, but these  
 411 details are beyond the scope of our simple bulk-plume model.

### 412 3.3.3 Linear response

416 The steady equations 14, 15, 16 and 17 do not constrain the (time-dependent) linear  
 417 response of our simple bulk-plume model. For simplicity, analytic tractability, and since the  
 418 moisture perturbations are small and free-tropospheric, we assume that the additional water  
 419 vapor behaves as a passive tracer to evaluate the response of our bulk-plume toy model. Note  
 420 that this approximation would not be valid in the boundary layer, as shown in panel (a) of  
 421 Figure 3, nor for large free-tropospheric perturbations that would inhibit or enhance deep  
 422 convection. This approximation ignores perturbations in the convective ensemble properties  
 423 ( $m, e, d, c$ ), which remain at their RCE values computed in section 3.3.2 during the linear  
 424 response. In a more realistic bulk-plume model, the transient evolution of the system would  
 425 depend on other equations, such as the mass-flux closure equation. We evaluate this passive  
 426 tracer linear response in four steps, following Figure 7:

- 427 1. We introduce a perturbation  $q'_j$  in a thin convecting layer  $[p_j - \Delta p/2, p_j + \Delta p/2]$ , with  
 428 entrainment:  $e_j = e(p_j)$ , where  $e$  is the RCE entrainment profile given by equation  
 429 19.
- 430 2. We assume that the perturbation  $q'_j$  is entrained into the convective plume at a rate  $e_j$   
 431 from the perturbation level  $p_j$  and this entrained portion of the water vapor perturba-  
 432 tion is communicated to all levels above:  $p_i < p_j$ .
- 433 3. At a given level  $p_i$  within the plume, the perturbation  $q'_j$  condenses at a rate propor-  
 434 tional to the local RCE condensation rate at that level:  $c_i = c(p_i)$ , and detrains at a  
 435 rate proportional to the RCE detrainment rate  $d_i q'_i = (dq^*)(p_i)$ . The proportionality  
 436 constant is uniform in the convecting layer and related to the entrainment rate at the  
 437 perturbation level.
- 438 4. Finally, the environmental perturbation is also advected downwards by the local subsi-  
 439 dence mass flux  $-m_i = -m(p_i)$ .

440 In appendix A.2, we show that the convective moistening response  $M_{\text{LH}}$  and the convective  
 441 heating response  $M_{\text{DSE}}$  are respectively given by:

$$(M_{\text{LH}})_{ij} = e_j \left[ \underbrace{-\delta_{ij}}_{\text{Entrained moisture}} + \underbrace{\frac{d_i q'_i \delta_{i>j}}{\sum_{i>j} (d_i q'_i + c_i)}}_{\text{Detrained moisture above}} \right] + \underbrace{\frac{g m_j [\delta_{i(j-1)} - \delta_{ij}]}{\Delta p}}_{\text{Downwards advection}}, \quad (23)$$

$$(M_{\text{DSE}})_{ij} = \underbrace{\frac{e_j \alpha_i c_i \delta_{i>j}}{\sum_{i>j} (d_i q'_i + c_i)}}_{\text{Latent heating above}}, \quad (24)$$

443 where  $\delta_{ij}$  is 0 if  $i \neq j$  and 1 if  $i = j$ ,  $\delta_{i>j}$  is 0 if  $i \leq j$  and 1 if  $i > j$ , and  $\delta_{j(i-1)}$  is 0 if  
 444  $i \neq j - 1$  and 1 if  $i = (j - 1)$ .

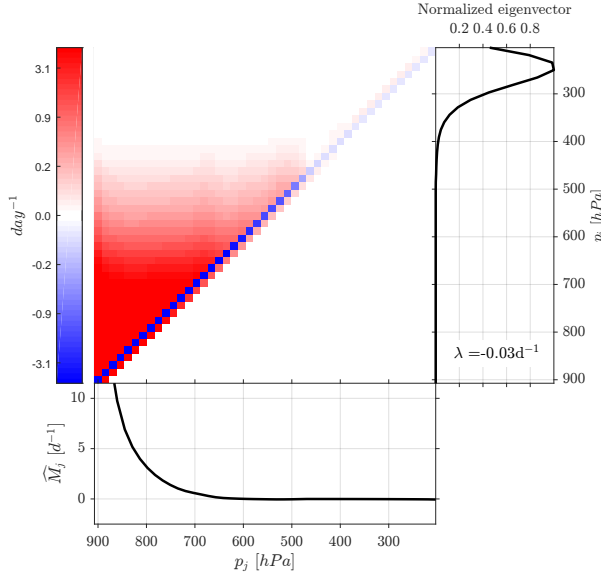
449 The linear convective response is depicted in Figure 8, while the separate convective  
 450 moistening and heating responses can be found in appendix A.2. Overall, the response of the  
 451 bulk-plume scheme to moist perturbations can be separated in three parts:

- 452 • A local drying (blue diagonal) due to the entrainment of water vapor in the plume and  
 453 its downwards advection by the subsiding mass flux.
- 454 • A growth of the perturbation above the perturbation level (red upper-left part of the  
 455 matrix) due to the detrainment of the moist plume as well as the latent heating within  
 456 the plume. This component of the response scales like the detrainment and condensa-  
 457 tion rate profiles from bottom to top, and like the local entrainment rate profile from  
 458 left to right.
- 459 • A moistening right below the perturbation level (red below the diagonal) due to the  
 460 downwards advection of the moist perturbation by the subsidence mass flux.

461 The Betts-Miller and bulk-plume convective responses both conserve moist static energy:  
 462 they locally damp the perturbation, and re-distribute it everywhere in the case of the Betts-  
 463 Miller scheme and upwards in the case of the bulk-plume scheme. Unlike convection, radia-  
 464 tion diabatically heats the column, which may enhance moist static energy perturbations even  
 465 when the HAM profile is uniform [e.g., *Beucler and Cronin, 2016*]).

#### 466 4 Linear response of radiation

467 In this section, we compute the linear response of longwave radiation  $M_{\text{LW}}$  and that of  
 468 shortwave radiation  $M_{\text{SW}}$  using analytical and real-gas radiative transfer models. We use the  
 469 same tropical basic state as in section 3.



445 **Figure 8.** Bulk-plume linear convective matrix ( $M_{\text{LH}} + M_{\text{DSE}}$ ) for  $\widehat{Q}_{\text{BP}} = 150 \text{ W m}^{-2}$ . (Bottom panel)  
 446 Vertically-integrated growth rate ( $\widehat{M}_j$  in  $\text{day}^{-1}$ ). (Right panel) Eigenvector corresponding to the leading  
 447 eigenvalue real part  $\lambda$ , normalized to have a maximum of 1 (note that the leading eigenvalue here is negative,  
 448 so it represents the slowest-decaying mode).

#### 470 4.1 Two-stream model of longwave radiation

471 The framework introduced here generalizes the analytical framework introduced in  
 472 *Beucler and Cronin* [2016] by allowing the water vapor profile to vary freely and writing  
 473 the differential optical thickness  $d\tau$  as a product of a general function  $f_1$  of pressure and a  
 474 general function  $f_2$  of specific humidity:

$$d\tau = \kappa f_1(p) f_2(q) \frac{dp}{g}, \quad (25)$$

475 where the gray longwave absorption coefficient  $\kappa$  has the units  $\text{m}^2 \text{ kg}^{-1}$ , and  $dp$  is the differ-  
 476 ential atmospheric pressure. *Beucler and Cronin* [2016] accounted for pressure broadening  
 477 of water vapor in a simple fashion by choosing  $\kappa = 0.17 \text{ m}^2 \text{ kg}^{-1}$ ,  $f_1(p) = p/p_s$ ,  $f_2(q) = q$ ,  
 478 where  $p_s$  is the surface pressure, and we make the same choice in this section. From the  
 479 two-stream Schwarzschild equation for a one-dimensional plane-parallel atmosphere (equa-  
 480 tions (10) and (11) of *Beucler and Cronin* [2016]), we can write the longwave convergence in  
 481 pressure coordinates  $d\mathcal{F}_{\text{LW}}/dp$  (in  $\text{W m}^{-2} \text{ hPa}^{-1}$ ) as the product of the longwave convergence  
 482 in optical thickness coordinates (in  $\text{W m}^{-2}$ ) with the differential optical thickness (in  $\text{hPa}^{-1}$ ):

$$\frac{d\mathcal{F}_{\text{LW}}}{dp} = \frac{d(\mathcal{F}_{\uparrow} - \mathcal{F}_{\downarrow})}{dp} = \underbrace{(\mathcal{F}_{\uparrow} + \mathcal{F}_{\downarrow} - 2\sigma T^4)}_{\text{LW convergence}} \overbrace{\frac{\kappa f_1 f_2}{g}}^{\text{Diff opt thickness}}, \quad (26)$$

484 where  $\mathcal{F}_{\uparrow}$  and  $\mathcal{F}_{\downarrow}$  are respectively the upwelling and downwelling radiative fluxes (in  $\text{W}$   
 485  $\text{m}^{-2}$ ),  $\sigma$  is the Stefan-Boltzmann constant and  $T$  is the atmospheric temperature. In ap-  
 486 pendix B.1, we show that the linear longwave response can be written as the sum of two

487 components:

$$(M_{\text{LW}})_{ij} = \frac{\kappa\alpha_i}{L_v} \underbrace{\left[ f_1 \left( \frac{df_2}{dq} \right)_{q=0} \right]_{p_j}}_{\text{Opt thick pert}} \left\{ \text{LW}_{\text{local},ij} + \overbrace{\frac{\kappa\Delta p (f_1 f_2)_{p_i}}{g}}^{\text{Local opt thickness}} \text{LW}_{\text{non-local},ij} \right\}. \quad (27)$$

488 Their general expression and physical interpretation for a moist perturbation  $q'_j > 0$  are:

- 489 1. A local increase in the radiative cooling, due to the increase of the local emissivity:

$$\text{LW}_{\text{local},ij} = \left( \mathcal{F}_{\uparrow} + \mathcal{F}_{\downarrow} - 2\sigma T^4 \right)_{p_i} \delta_{ij}, \quad (28)$$

- 490 2. A non-local term that has different signs above and below the perturbation:

$$\text{LW}_{\text{non-local},ij} = \underbrace{\exp(-|\tau_i - \tau_j|)}_{\text{Transmissivity}} \left[ -(\mathcal{F}_{\uparrow})_{p_j} \delta_{i>j} - (\mathcal{F}_{\downarrow})_{p_j} \delta_{i<j} + \sigma T_j^4 \delta_{i \neq j} \right], \quad (29)$$

491 where  $\tau_i$  is the optical thickness of the atmosphere between  $p_i$  and space,  $\tau_j$  is the  
 492 optical thickness of the atmosphere between  $p_j$  and space, and  $T_j$  is the atmospheric  
 493 temperature at the perturbation level. Above the perturbation level ( $i > j$ ), the up-  
 494 welling flux received from the perturbation  $(\mathcal{F}_{\uparrow})_{p_j}$  decreases because the moist pertur-  
 495 bation absorbs some of the upwelling atmospheric radiation below it. Below the per-  
 496 turbation level ( $i < j$ ), the downwelling flux received from the perturbation  $(\mathcal{F}_{\downarrow})_{p_j}$  decreases  
 497 because the moist perturbation absorbs some of the downwelling atmospheric radia-  
 498 tion above it. In return, the perturbation emits radiative energy up and down at a rate  
 499  $\sigma T_j^4$ . Because the atmospheric temperature decreases with height, the emission term  
 500  $\sigma T_j^4$  exceeds the radiative flux  $(\mathcal{F}_{\downarrow})_{p_j}$  received from above but is less than the radia-  
 501 tive flux  $(\mathcal{F}_{\uparrow})_{p_j}$  received from below. Therefore, we expect the net longwave conver-  
 502 gence to decrease above the perturbation level and to increase below it for a positive  
 503 moisture perturbation. The amplifying radiative linear response resulting from the  
 504 non-local heating perturbation below a moist perturbation (or cooling perturbation  
 505 below a dry perturbation) is referred to as the radiative amplification effect.

506 Figure 9a shows the longwave linear response for a surface optical thickness of 5.4, which  
 507 matches the net radiative cooling as computed in SAM and is a reasonable tropical value cor-  
 508 responding to column water vapor values of  $40 \text{ kg m}^{-2}$  in the simple model of *Beucler and*  
 509 *Cronin* [2016]. The local increase is cooling ( $\text{LW}_{\text{local}}$ ) appears as a blue diagonal through-  
 510 out the troposphere, except near the tropopause where the gray-radiation skin temperature  
 511 exceeds the atmospheric temperature, leading to local heating and pointing to one limitation  
 512 of the gray model. The decrease in radiation received from the ground is prevalent in the  
 513 lower troposphere, and corresponds to the blue area above the bottom left corner of the ma-  
 514 trix. The damping linked to the decrease in radiation received from the atmosphere is largest  
 515 right above and right below the diagonal, and explains why the blue zone above the diagonal  
 516 extends to the mid-troposphere. The radiative amplification term is larger than the damp-  
 517 ing terms and well-distributed below the perturbation level. Water vapor molecules below a  
 518 moist perturbation emit less radiation to space, resulting in a net heating below the perturba-  
 519 tion level. For lower-tropospheric perturbations, the three damping terms on the right-hand  
 520 side of equation 27 are prevalent in the sum, and  $\hat{M}_j < 0$ . However,  $\hat{M}_j$  becomes positive  
 521 in the case of mid to upper-tropospheric perturbations, for which the radiative amplification  
 522 term is largest. The potential growth of column-integrated perturbations through their unsta-  
 523 ble interaction with longwave radiation has been extensively studied in *Beucler and Cronin*  
 524 [2016], and referred to as moisture-radiative cooling instability. Note that the toy radiative

525 model presented in equation 28 of *Emanuel et al.* [2014] is a specific case of our gray model  
 526 in the limit of two optically-thin atmospheric layers. This framework provides fundamental  
 527 understanding for the gray part of the clear-sky real-gas radiative response, and gives an idea  
 528 of the cloud longwave radiative response, for which the gray approximation holds better. The  
 529 reader interested in the assumptions made in order to compute the optical thickness profile  
 530 for Figure 9 is referred to appendix B.3.

## 531 4.2 One-stream model of shortwave radiation

532 Following *Beucler and Cronin* [2016], we adopt a simple one-stream model of radia-  
 533 tion with the generalized optical thickness given by equation 25:

$$\mathcal{F}_{\text{SW}} = \mathcal{S}e^{-\varepsilon\tau}, \quad (30)$$

534 where  $\mathcal{F}_{\text{SW}}$  is the downwelling shortwave flux (in  $\text{Wm}^{-2}$ ),  $\mathcal{S}$  the solar constant,  $\tau$  the optical  
 535 thickness and  $\varepsilon$  the factor relating the longwave to shortwave optical thickness. Assuming  
 536 that  $\varepsilon$  does not vary with pressure to first order, the shortwave flux convergence is simply  
 537 given by:

$$-\frac{d\mathcal{F}_{\text{SW}}}{dp} = \underbrace{\frac{\kappa\varepsilon f_1 f_2}{g}}_{\text{Diff opt thickness}} \mathcal{F}_{\text{SW}}. \quad (31)$$

538 In appendix B.2, we show that the linear shortwave response can be written as the sum of  
 539 two terms:

$$(M_{\text{SW}})_{ij} = \frac{\kappa\alpha_i (\mathcal{F}_{\text{SW}})_{p_i}}{L_v} \underbrace{\left[ \varepsilon f_1 \left( \frac{df_2}{dq} \right)_{q=0} \right]_{p_j}}_{\text{Opt thick pert}} \left[ \begin{array}{ccc} & \text{Local opt thickness} & \\ \underbrace{\delta_{ij}}_{\uparrow \text{Local emissivity}} & - \frac{\kappa\Delta p \cdot \varepsilon \cdot (f_1 f_2)_{p_i}}{g} & \underbrace{\delta_{i < j}}_{\downarrow \text{Rad received}} \end{array} \right], \quad (32)$$

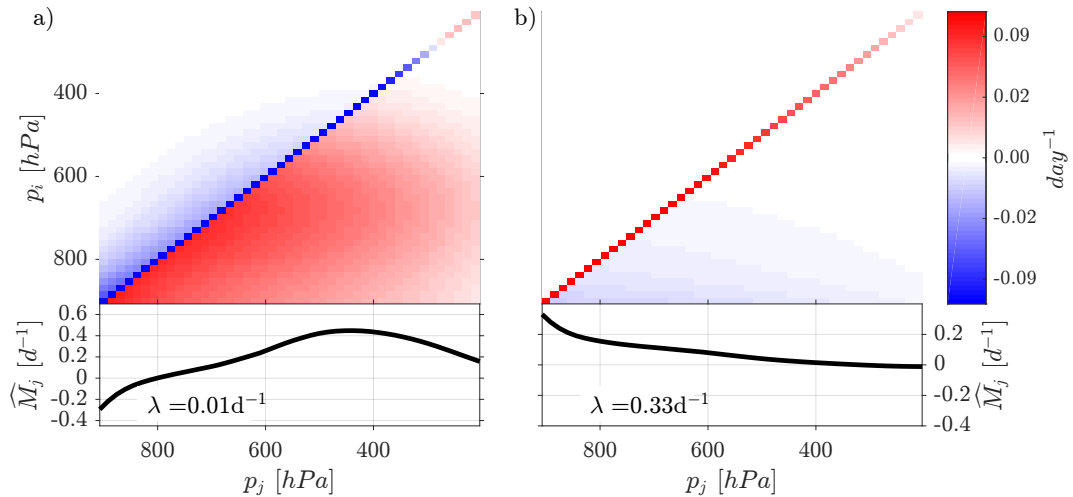
- 540 1. A local increase in the radiative heating, due to the increase of the local emissivity.
- 541 2. A decrease in the solar radiation received below the perturbation level.

542 The shortwave linear response matrix is depicted in Figure 9b. The local increase in radia-  
 543 tive heating corresponds to the red diagonal and is attenuated by the decrease in received  
 544 solar radiation below the perturbation level. Because the atmosphere is optically thin in the  
 545 shortwave, the strength of the linear response is mostly affected by the local value of the  
 546 product  $\alpha f_1$ , which increases strongly with pressure. Therefore,  $\widehat{M}_j$  is greatest in the lower  
 547 troposphere and quickly decays for higher perturbations. Although the gray model qualita-  
 548 tively exhibits the basic physics of the linear radiative response, different water vapor spectral  
 549 bands saturate at different humidity levels, and we use of a full radiative model in order to  
 550 yield accurate results in section 4.3.

## 557 4.3 Real-gas radiative transfer

### 558 4.3.1 Method

559 In order to take into account the full water vapor absorption spectrum, we use the  
 560 RRTMG model *Iacono et al.* [2000, 2008]; *Mlawer et al.* [1997] to compute the response  
 561 of the atmosphere to small water vapor perturbations. Following *Beucler and Cronin* [2016],  
 562 we use version 4.85 of the longwave and version 3.9 of the shortwave column versions of  
 563 RRTMG, a broadband, two-stream, correlated k-distribution radiative transfer model, that  
 564 has been tested against line-by-line radiative transfer models. The RCE water vapor and tem-  
 565 perature profiles are once again the observed January SAM RCE profiles, and have 60 levels  
 566 in the vertical. To match the clear-sky radiative transfer of the SAM base state as closely as



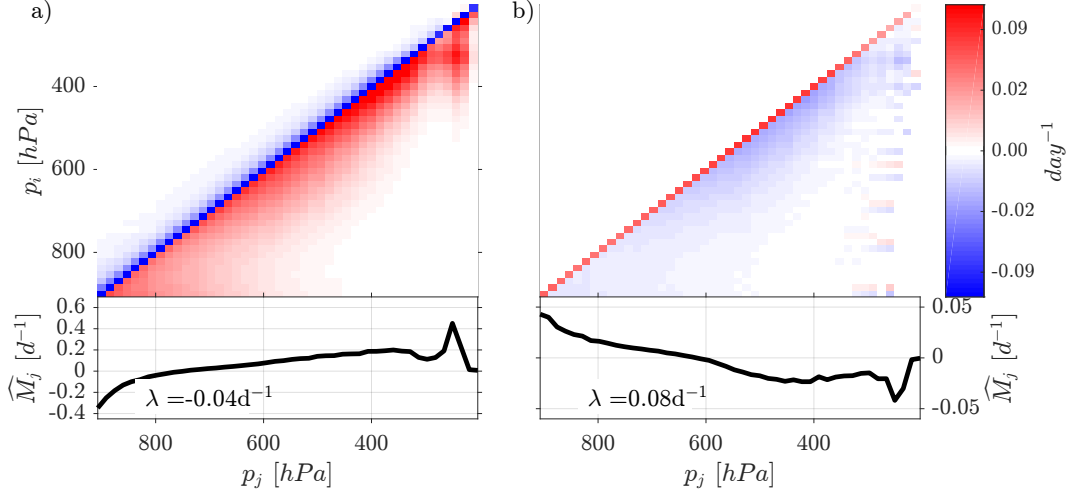
551 **Figure 9.** (a) Longwave linear response matrix (in month<sup>-1</sup>) and vertically integrated longwave growth rate  
 552 (in day<sup>-1</sup>) plotted against perturbation level (in hPa). (b) Shortwave linear response and vertically integrated  
 553 shortwave growth rate. The total optical thickness of the free troposphere is 6 in the longwave and 0.5 in the  
 554 shortwave. It corresponds to a net free-tropospheric cooling of 215 W m<sup>-2</sup>. The analytical matrices, with  
 555 leading real eigenvalues  $\lambda$ , have both been tested against a numerical version of the two-stream Schwarzschild  
 556 model.

567 possible, we also specify a constant carbon dioxide mixing ratio of 355ppmv and use the  
 568 standard SAM tropical ozone mixing ratio profile depicted in Figure 4d. The solar zenith angle  
 569 is chosen to be  $\arccos(\pi/4)$  rad, the insolation-weighted equatorial equinox value. The  
 570 linear radiative responses are obtained in 4 steps:

- 571 1. We use RRTMG in order to compute the structure of the longwave and shortwave  
 572 radiative fluxes from the RCE greenhouse gas and temperature profiles.
- 573 2. We perturb the RCE water vapor profile level by level. 64 “moistened” profiles are  
 574 produced, by adding 1% to the specific humidity at each level. Similarly, 64 “dried”  
 575 profiles are produced by removing 1% from the RCE specific humidity at each level.
- 576 3. For each perturbed profile, we use RRTMG to compute the structure of longwave and  
 577 shortwave radiative fluxes. We multiply the shortwave fluxes by a constant factor to  
 578 account for the diurnal cycle and match the total shortwave heating in SAM (the fac-  
 579 tor is close to  $4/\pi^2$ , which would exactly account for an insolation-weighted zenith  
 580 angle).
- 581 4. By subtracting the RCE radiative fluxes to the perturbed radiative fluxes, we obtain  
 582 the perturbation radiative fluxes, from which we compute the longwave and shortwave  
 583 linear responses matrices following equations 3 and 6.

### 584 4.3.2 Results

589 The longwave and shortwave linear response matrices are respectively depicted in  
 590 Figure 10a and 10b. The total radiative linear response matrix is qualitatively similar to the  
 591 clear-sky radiative responses obtained by *Emanuel et al.* [2014] for a negative moisture per-  
 592 turbation, with a radiative amplification effect concentrated below the diagonal that expands  
 593 as surface temperature increases. For the SAM RCE reference profile, the total longwave ra-



585 **Figure 10.** (a) Longwave linear response matrix (in month<sup>-1</sup>) and vertically integrated longwave growth  
 586 rate (in day<sup>-1</sup>) plotted against perturbation level (in hPa). (b) Shortwave linear response and vertically in-  
 587 tegrated shortwave growth rate. The HAM has been evaluated from the reference SAM RCE profile. The  
 588 leading real eigenvalue  $\lambda$  of each matrix is indicated in the corresponding bottom panel.

594 diative cooling is  $211 \text{ W m}^{-2}$  and the total shortwave radiative heating  $61 \text{ W m}^{-2}$ , leading to  
 595 a net cooling of  $150 \text{ W m}^{-2}$ , which is the standard value we use for  $\hat{Q}_{\text{BP}}$  in the bulk-plume  
 596 model (section 3.3). The vertically-integrated response is negative for lower-tropospheric  
 597 perturbations, and grows as the longwave amplification effect becomes larger to values of  
 598 order  $0.5 \text{ day}^{-1}$  for perturbations near the tropopause. The shortwave effect is opposite and  
 599 reaches  $-0.05 \text{ day}^{-1}$  for perturbations near the tropopause. The main difference when going  
 600 from a gray-gas to a real-gas model of radiation is the sharp amplification of the response  
 601 growth rates near the tropopause. There, the most absorbing bands of water vapor (large  $\kappa$ )  
 602 contribute to longwave cooling and shortwave heating. Therefore, small water vapor pertur-  
 603 bations will change the optical thickness by a greater amount per unit mass perturbation in  
 604 water vapor amount.

## 605 5 Linear evolution of small water vapor perturbations

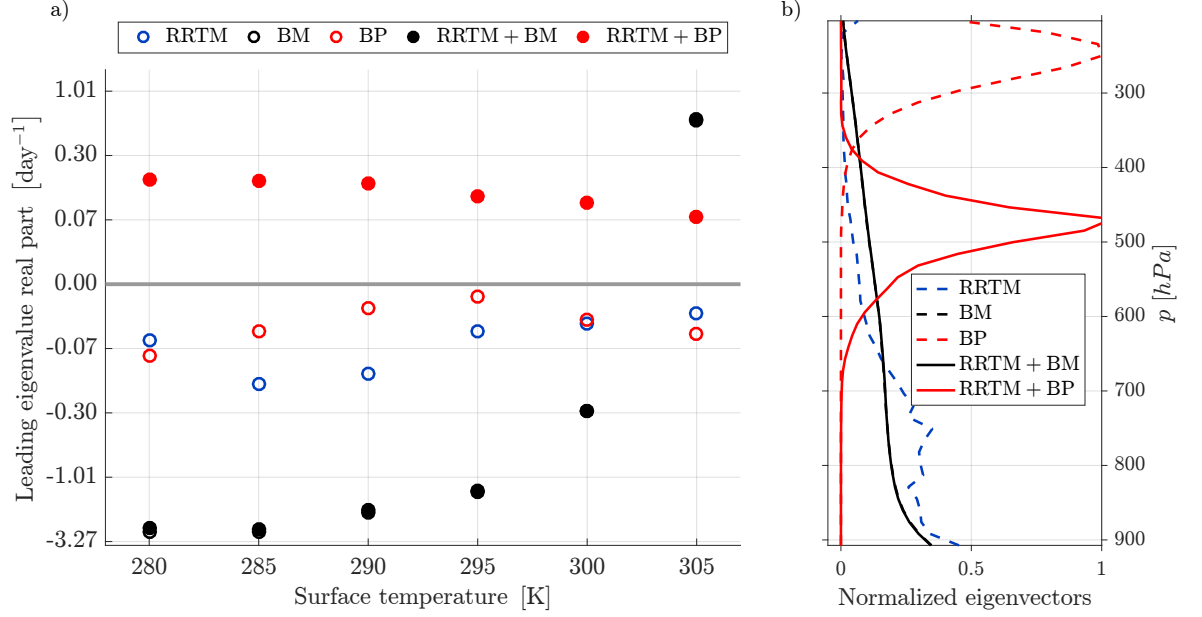
606 In this section, we combine the Betts-Miller convective response (referred to as BM,  
 607 see section 3.2) and the bulk-plume convective response (referred to as BP, see section 3.3)  
 608 with the real-gas radiative response (referred to as RRTM, see section 4.3), in order to obtain  
 609 the full linear response and study the linear evolution of small water vapor perturbations.  
 610 The total Betts-Miller response matrix  $M_{\text{BM+RRTM}}$  and the total bulk-plume response matrix  
 611  $M_{\text{BP+RRTM}}$  are given by:

$$M_{\text{BM+RRTM}} = M_{\text{BM}} + M_{\text{RRTM}}, \quad (33)$$

612

$$M_{\text{BP+RRTM}} = M_{\text{BP}} + M_{\text{RRTM}}, \quad (34)$$

613 where  $M_{\text{BM}}$  is the Betts-Miller convective response (sum of the responses given by equa-  
 614 tions 12 and 13) for the Betts-Miller timescale  $\tau_{\text{BM}} = 3h$ ,  $M_{\text{BP}}$  is the bulk-plume convective  
 615 response (sum of the responses given by equations 23 and 24) for the radiative cooling pa-  
 616 rameter computed from the RRTM model, and  $M_{\text{RRTM}}$  is the RRTM radiative response (sum  
 617 of the longwave and shortwave responses shown in Figure 10). We show in Appendix C that



620 **Figure 11.** (a) Leading eigenvalue real part (in day<sup>-1</sup>) as a function of the RCE surface temperature (in K).  
 621 (b) Corresponding eigenvectors for the 300K reference case: Radiative response alone (RRTM), Betts-Miller  
 622 response alone (BM,  $\tau_{\text{BM}} = 3$  hours), bulk-plume response alone (BP,  $\widehat{Q}_{\text{BP}} = 150 \text{ W m}^{-2}$ ), and their sums  
 623 (RRTM+BP) & (RRTM+BM). The lines for (BM) and (RRTM+BM) are indistinguishable. The eigenvectors  
 624 have been normalized to have the same pressure-average.

618 the results of this section are robust across a wide range of convective parameters  $\tau_{\text{BM}}$  and  
 619  $\widehat{Q}_{\text{BP}}$ .

625 From section 2.1, we remember that the linear response matrix may be linearly un-  
 626 stable if its leading eigenvalue real part is greater than zero. In Figure 11a, we compute the  
 627 leading eigenvalue real part of each matrix for different values of the surface temperature:

- 628 • (RRTM) For the reference SAM RCE profile, the leading eigenvalue real part corre-  
 629 sponds to a decay time scale of 27 days; there is no pure linear instability from radi-  
 630 ation alone. Because the radiative linear response matrix is mostly lower triangular,  
 631 with a strictly negative diagonal corresponding to strong local cooling, water vapor  
 632 perturbations are displaced downwards and eventually damped out in the absence  
 633 of convection, though they may initially amplify as they are displaced through non-  
 634 normal growth. Except for the 280K case, the decay timescale increases with temper-  
 635 ature, suggesting that the clear-sky radiation's damping effect is less pronounced in  
 636 warmer climates. Finally, we find that the clear-sky radiative feedback can be linearly  
 637 unstable if the RCE relative humidity profile is artificially dried, due to the upper-  
 638 tropospheric radiative amplification effect. For readability purposes, the results are  
 639 not shown in Figure 11 but provided to the reader in the corresponding MATLAB  
 640 script.
- 641 • (BM) In the WTG framework, Betts-Miller convection is linearly unstable if and only  
 642 if the mean free-tropospheric HAM is larger than 1 (analogous to a negative gross  
 643 moist stability). This condition is only satisfied for the 305K simulation, in which the  
 644 specific humidity remains above 5g/kg and the HAM remains above 1 in the lower  
 645 troposphere (see panels a and c of figure 4). In the unstable case (305K), the pertur-  
 646 bation latent heating in the lower troposphere induces strong upward motion because

647  $\alpha > 1$  there, leading to the unstable growth of lower to mid-tropospheric water vapor  
 648 perturbations. In the stable case (all cases but 305K), these perturbations are damped  
 649 because a larger mass of the atmosphere has:  $\alpha < 1$ , which makes the convective dry-  
 650 ing effect overcome the latent heating effect. Mathematically, we prove in appendix  
 651 A.3 that the leading eigenvalue real part of the Betts-Miller linear response is propor-  
 652 tional to the vertical average of HAM minus 1 (see equation .9), which increases with  
 653 surface temperature as can be seen on figure 11. This growth rate is exactly reached  
 654 for a water vapor perturbation profile that is proportional to the HAM profile.

- 655 • (RRTM+BM) Adding the radiative response reinforces the local and upper-tropospheric  
 656 perturbation's damping. However, the stability of the combined linear response matrix  
 657 is barely distinguishable from that of the convective response alone for Betts-Miller  
 658 timescales as short as 3 hours.
- 659 • (BP) The bulk-plume response is mostly upper triangular, with a strictly negative  
 660 diagonal corresponding to local drying through the entrainment of the water vapor  
 661 perturbation. The decay timescale of the bulk-plume convective response is approxi-  
 662 mately equal to the minimal entrainment value, as the leading eigenvalue real part is  
 663 close (within  $\sim 20\%$  in our case) to  $-\min_p [e(p)]$ , where  $e$  is the entrainment profile  
 664 (see appendix A.3). Therefore, bulk-plume convection is always linearly stable on its  
 665 own. The dependence of the leading eigenvalue real part on surface temperature is  
 666 weak, consistent with the weak dependence of the entrainment minimum on surface  
 667 temperature.
- 668 • (RRTM+BP) The combination of the bulk-plume convective response with the ra-  
 669 diative response is linearly unstable for all surface temperatures. Physically, lower-  
 670 tropospheric perturbations are carried upwards by the plume where they can reinforce  
 671 through the radiative amplification effect identified in equation 29. Upper-tropospheric  
 672 perturbations can also amplify mid-tropospheric perturbations through radiative am-  
 673 plification, which are then carried upwards in the plume. Mathematically, the combi-  
 674 nation of an upper and a lower triangular matrices with positive off-diagonal values  
 675 can allow part of the spectrum to become positive.

676 The leading eigenvalue real part informs us about the linear growth rate of each re-  
 677 sponse matrix. We now focus on the vertical structure of water vapor perturbations. The  
 678 evolution of a given perturbation can be found by exponentiating the linear response matrix,  
 679 following equation 8. If we compute the growth rate of column water vapor perturbations,  
 680 we find that the leading eigenvalue real part can be used as a predictor of the order of mag-  
 681 nitude of the growth rate on a time scale of order days. For the first few hours, the transient  
 682 growth rate of water vapor perturbations is very dependent on their initial shape. After a few  
 683 days, dominant vertical modes appear, which mathematically correspond to the eigenvectors  
 684 associated with the leading eigenvalue real part of each convective response. These eigen-  
 685 vectors, depicted in Figure 11b, are the HAM profile for  $M_{BM}$  and an upper tropospheric  
 686 bulge for  $M_{BP}$ ; they grow at a rate given by the corresponding leading eigenvalue real parts  
 687  $\lambda_{BM}$  and  $\lambda_{BP}$ . In contrast, the purely radiative response (RRTM) damps the perturbation in  
 688 the upper troposphere, as radiative cooling is increased above the perturbation level, and in  
 689 the lower troposphere, where the radiative amplification term is smallest. When combined  
 690 with Betts-Miller convection (RRTM+BM), radiation slightly damps the upper-tropospheric  
 691 perturbation, which can not be seen by eye in Figure 11b. However, the bulk-plume scheme  
 692 moves the moist lower-tropospheric perturbation upwards in the mid-troposphere, where the  
 693 radiative amplification effect is largest. This means that the perturbation grows faster when  
 694 bulk-plume convection and radiation are added (RRTM+BP). The perturbation decays in the  
 695 lower troposphere, where it is entrained upwards, and in the upper troposphere, where it is  
 696 advected downwards. In both cases, the convection scheme dominates the pattern of vertical  
 697 moisture perturbation response. Thus, the (RRTM+BM) & (BM) eigenvectors are indistin-  
 698 guishable, while the (RRTM+BP) & (BP) eigenvectors are close in the lower troposphere.  
 699 As a closing point, we remind the reader that these eigenvectors are all computed in terms of

specific humidity; eigenvectors expressed in terms of relative humidity would in all cases be strongly weighted towards the upper troposphere, where the reference-state  $q$  is small.

## 6 Conclusion

In section 2, we developed a theoretical framework to compute the response of RCE to small water vapor perturbations in WTG: The resulting linear response function (equation 5) is the sum of the convective moistening, convective heating, longwave heating and shortwave heating linear response functions. The linear response function can be represented as a two-dimensional matrix (equation 9), which can be exponentiated in order to compute the evolution of water vapor perturbations for short times. In section 3, we calculated analytic responses of two toy models of the convective linear response: a Betts-Miller-like scheme, which re-distributes a local moisture perturbation to the rest of the atmosphere in the form of convective heating, and a bulk-plume-like scheme, which sends a moisture perturbation upwards. Comparing our responses with those obtained by *Kuang* [2012] (Figures 8c and 8d), the Betts-Miller response is similar to the response of a cloud-permitting model in an elongated domain (aspect ratio larger than 20), whereas the response of the same model in a square domain resembles the bulk-plume response. Additionally, the convective response studied in section 3.1.1 presents characteristics of both convective toy models, as confirmed by its eigenmode peaking at 575hPa (right panel of figure 3), which is the arithmetic mean of the bulk-plume's mode 250hPa peak and the Betts-Miller's mode 900hPa peak (right panel of figure 11). This suggests that the physical insight obtained in section 3 could be used to understand the more intricate physics of cloud resolving model responses. In section 4, we investigated the physics of the clear-sky radiative response using the Schwarzschild equations. The response includes a local damping of moisture perturbations and a radiative amplification effect of mid-tropospheric perturbations in the lower troposphere. We also quantitatively evaluated the clear-sky response by using a real-gas radiative transfer model, and found large non-gray radiative feedbacks in the upper troposphere. Section 5 shows that despite the damping effect of the radiative response, it could amplify the unstable convective response in the bulk-plume case. In contrast, the Betts-Miller response's stability depends on the mean free-tropospheric HAM, which increases with temperature, causing linear instability above surface temperatures of 300K.

Although this work explores the physics of the interaction between water vapor, convection and clear-sky radiation in depth, two critical elements of the response are lacking: the cloud response and the surface temperature response. The first requires knowledge of how cloudiness responds to water vapor perturbations (which is mediated by convection and also depends on microphysical factors such as the background cloud condensation nuclei profile) and of how cloudiness affects the radiative heating profile. Preliminary results indicate that the cloud longwave response significantly enhances the longwave radiative amplification effect described in this study, making RCE more prone to linear instability. The second is an air-sea interaction problem, exploring the interaction between atmospheric moisture and surface temperature gradients, which could be relevant for monsoonal intraseasonal oscillations [e.g., *Sengupta et al.*, 2001; *Vecchi and Harrison*, 2002] and help better understand coupled general circulation model results [e.g., *Coppin and Bony*, 2017].

This work connects with results from convection-permitting modeling by showing that despite the robustness of radiative thermodynamic feedbacks, the evolution and structure of water vapor perturbations is extremely sensitive to the linear response of convection. Even when convection is not parameterized, its linear response can differ greatly across model geometries [*Kuang*, 2012], and this may connect with the known sensitivity of aggregation to many aspects of convection-permitting model setup, including resolution and subgrid parameterizations [e.g., *Muller and Held*, 2012; *Tompkins et al.*, 2017]. Our findings may thus help to explain why the self-aggregation of convection in cloud-permitting models is finicky: the convective linear response is critical, and we still do not fully understand what controls it. Decomposing the full linear response into a Betts-Miller-type response, a bulk-plume-type

752 response (using the mean HAM profile), and a radiative response could provide insight into  
 753 the early stages of self-aggregation and help explain why the peak of the main moisture mode  
 754 can be found in the mid-troposphere.

## 755 **Appendix A: Linear response of the bulk-plume equations**

### 756 **A.1. Basic state**

757 In order to eliminate the variations of the updraft mass flux  $m$  with pressure  $p$ , we com-  
 758 bine equations 19, 20 and 21 with equation 18:

$$gm \frac{\partial q^*}{\partial p} = c + eq_{\text{def}}, \quad (1)$$

$$759 \quad gm \frac{\partial q}{\partial p} = dq_{\text{def}}, \quad (2)$$

$$760 \quad gm \frac{\partial (s + L_v q^*)}{\partial p} = L_v eq_{\text{def}}, \quad (3)$$

761 where we have assumed that the in-cloud dry static energy was equal to the environmen-  
 762 tal dry static energy (neutral buoyancy assumption) and introduced the saturation deficit  
 763  $q_{\text{def}}$  defined in equation 22. Subtracting equation .3 to equation .2 and using equation 18  
 764 leads to a first order differential equation for the updraft mass flux:

$$\frac{1}{m} \frac{\partial m}{\partial p} = -\frac{1}{q_{\text{def}}} \left( \frac{\partial q_{\text{def}}}{\partial p} + \frac{1}{L_v} \frac{\partial s}{\partial p} \right). \quad (4)$$

765 The vertically integrated energetic balance requires that the free-tropospheric convective  
 766 heating (equal to the convective flux at the top of the boundary layer) balances the free-  
 767 tropospheric radiative cooling  $\widehat{Q}_{\text{BP}} > 0$ :

$$\frac{L_v}{g} \int_{p_b}^P c = L_v m(p_b) q_{\text{def}}(p_b) = \widehat{Q}_{\text{BP}},$$

768 leading to the unique solution 18 for the updraft mass flux, as long as the free troposphere is  
 769 not saturated in RCE ( $\forall p, q < q^*$ ). The entrainment, detrainment and condensation rates can  
 770 be obtained by combining equations .3, .2 and .1 to equation 18.

### 771 **A.2. Linear response**

772 In order to compute the convective moistening and heating resulting from the moist  
 773 perturbation  $q'_j$ , we follow the steps listed in section 3.3.3:

- 774 • Step 3: The convective drying tendency due to the entrainment of the moist perturba-  
 775 tion in the plume can be written:

$$\left( \frac{dq'_i}{dt} \right)_{\text{Ent}} = -e_j q'_j \delta_{ij}. \quad (5)$$

- 776 • Step 4: The convective moistening due to the detrainment of water vapor from the  
 777 plume (above the perturbation level) is:

$$\left( \frac{dq'_i}{dt} \right)_{\text{Det}} = C_{\text{Det}} e_j q'_j d_i q_i^* \delta_{i>j}, \quad (6)$$

778 while the convective heating due to the condensation of water vapor in the plume  
779 (above the perturbation level) is:

$$L_v \left( \frac{dq'_i}{dt} \right)_{\text{Con}} = C_{\text{Con}} e_j q'_j c_i \delta_{i>j}, \quad (.7)$$

780 where  $C_{\text{Det}}$  and  $C_{\text{Con}}$  are proportionality constants. We have assumed that these two  
781 constants were equal ( $C_{\text{Det}} = C_{\text{Con}} = C$ ). Using the conservation of the water vapor  
782 perturbation  $q'_j$  yields:

$$\left( \frac{dq'_i}{dt} \right)_{\text{Ent}} = \sum_{i>j} \left[ \left( \frac{dq'_i}{dt} \right)_{\text{Det}} + \left( \frac{dq'_i}{dt} \right)_{\text{Con}} \right] \quad (.8)$$

783 Combining equations .5, .6, .7 and .8 allows us to express the proportionality constant  
784  $C$  as a function of the detrainment and condensation rates:

$$C = \frac{1}{\sum_{i>j} (d_i q'_i + c_i)}.$$

785 • Step 5: The downwards advection of the perturbation by the subsidence mass flux can  
786 be written using an upwind advection scheme. At the perturbation level ( $i = j$ ):

$$\left( \frac{dq'_i}{dt} \right)_{\text{Adv}} = -q'_j \frac{gm_j}{\Delta p} \delta_{ij},$$

787 while below the perturbation level ( $i = j - 1$ ):

$$\left( \frac{dq'_i}{dt} \right)_{\text{Adv}} = q'_j \frac{gm_j}{\Delta p} \delta_{i(j-1)}.$$

788 The full convective moistening response (equation 23) and convective heating response  
789 (equation 24) are then computed by using their definition:

$$(M_{\text{LH}})_{ij} = \frac{1}{q'_j} \left[ \left( \frac{dq'_i}{dt} \right)_{\text{Ent}} + \left( \frac{dq'_i}{dt} \right)_{\text{Det}} + \left( \frac{dq'_i}{dt} \right)_{\text{Adv}} \right],$$

790

$$(M_{\text{DSE}})_{ij} = \frac{\alpha_i}{q'_j} \left( \frac{dq'_i}{dt} \right)_{\text{Con}}.$$

793 Because of the limits of our simple bulk-plume model, the entrainment rate is negative  
794 right above the top of the boundary layer and in parts of the upper troposphere, which would  
795 yield inconsistent linear responses. This problem is addressed by replacing the negative val-  
796 ues of  $e_j$  with the closest positive value of the entrainment rate that can be found below the  
797 level  $p_j$ .

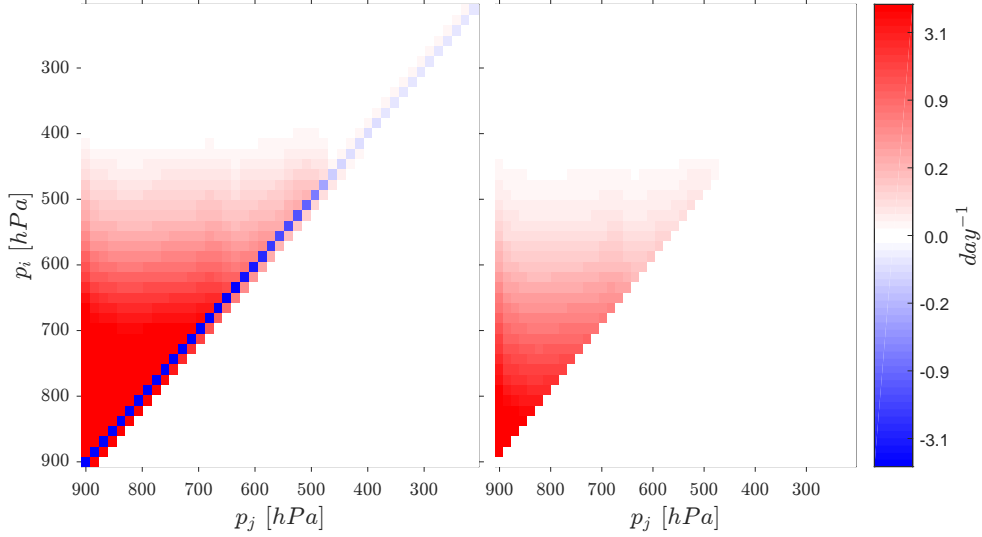
### 798 A.3. Leading eigenvalue of the convective response matrices

799 We approximate the spectrum of the bulk-plume linear response matrix  $M_{\text{BP}}$  (sum of  
800 the responses given by equations 23 and 24) by the spectrum of the upper triangular matrix  
801 with the following diagonal:

$$(M_{\text{BP}})_{ii} + (M_{\text{BP}})_{(i-1)i} = -e_i.$$

802 In practice, this approximation is justified when the size of  $M_{\text{BP}}$  is large enough for its neigh-  
803 boring diagonal coefficients to be close:

$$|(M_{\text{BP}})_{ii} - (M_{\text{BP}})_{(i+1)(i+1)}| \ll |(M_{\text{BP}})_{ii}|.$$



791 **Figure .12.** (a) Convective moistening ( $M_{LH}$ ) and (b) Convective heating ( $M_{DSE}$ ) linear response matrices,  
 792 in units  $\text{day}^{-1}$ .

804 The spectrum of an upper triangular matrix is given by its diagonal values:  $e_i > 0$ , which  
 805 means that the leading eigenvalue real part of the bulk-plume linear response  $\lambda_{BP}$  is approxi-  
 806 mately given by:

$$\lambda_{BP} \approx -\min_p [e(p)].$$

807 For completeness, we compute the leading eigenvalue of the Betts-Miller linear response  
 808  $M_{BM}$  (sum of the responses given by equations 12 and 13). According to Gershgorin circle  
 809 theorem, the spectrum of  $M_{BM}$  lies in the disc of center:

$$(M_{BM})_{ii} = \frac{1}{\tau_{BM}} \left( -1 + \frac{\alpha_i \Delta p}{p_b - p_t} \right),$$

810 and radius:

$$R_i = \sum_{j \neq i} |(M_{BM})_{ij}| = \frac{\Delta p}{\tau_{BM} (p_b - p_t)} \sum_{j \neq i} \alpha_j.$$

811 Therefore, an upper bound for the real part of the spectrum of  $M_{BM}$  is:

$$\lambda_{BM} = (M_{BM})_{ii} + R_i = \frac{1}{\tau_{BM}} \left( \underbrace{\frac{\Delta p}{p_b - p_t} \sum_j \alpha_j}_{\text{Vertical average } \alpha} - 1 \right). \quad (9)$$

812 This upper bound is reached for the eigenvector  $\alpha_i$ , which proves that  $\lambda_{BM}$  is the exact lead-  
 813 ing eigenvalue real part of the Betts-Miller linear response.

814 **Appendix B: Linear response of the Schwarzschild equations**

 815 **B.1. Two-stream model of longwave radiation**

816 First, we linearize the longwave flux convergence, given by equation 26, about RCE:

$$\frac{g}{\kappa} \frac{d\mathcal{F}_{\text{LW}}'}{dp} = f_1 f_2' (\mathcal{F}_{\uparrow} + \mathcal{F}_{\downarrow} - 2\sigma T^4) + f_1 f_2 (\mathcal{F}_{\uparrow}' + \mathcal{F}_{\downarrow}') \quad , \quad (10)$$

817 To quantitatively evaluate the second term of equation .10, we can:

- 818 1. Perturb the analytical solutions computed in
- Beucler and Cronin*
- [2016] about RCE.
- 
- 819 2. Use fundamental properties of the two-stream Schwarzschild equations, written be-
- 
- 820 low:

$$\frac{d\mathcal{F}_{\uparrow}}{d\tau} = \mathcal{F}_{\uparrow} - \sigma T^4 \quad , \quad \frac{d\mathcal{F}_{\downarrow}}{d\tau} = -\mathcal{F}_{\downarrow} + \sigma T^4. \quad (11)$$

 821 The first method is straightforward but mathematically technical; here we adopt the second  
 822 method to gain physical insight into gray radiative transfer. Let's start with the upwelling flux  
 823  $\mathcal{F}_{\uparrow}$  and integrate its Schwarzschild equation from the optical thickness  $\tau_j$  of a level  $p_j$  to the  
 824 optical thickness  $\tau_i$  of a level  $p_i$ :

$$\underbrace{(\mathcal{F}_{\uparrow})_{\tau_i}}_{\text{Flux i}} = \underbrace{e^{-(\tau_j - \tau_i)}}_{\text{Transmittivity i} \rightarrow \text{j}} \left[ \underbrace{(\mathcal{F}_{\uparrow})_{\tau_j}}_{\text{Flux j}} + \underbrace{\sigma \int_{\tau_i}^{\tau_j} T^4 e^{-\tau'} d\tau'}_{\text{Atm emission i} \rightarrow \text{j}} \right]. \quad (12)$$

 825 We now introduce an optical thickness perturbation  $\tau_j'$  around the level  $p_j$  by introducing  
 826 a water vapor perturbation  $q_j'$  in a thin pressure layer  $[p_j - \Delta p/2, p_j + \Delta p/2]$  for which  
 827  $\Delta p \ll p_j$ . Our goal is to find the radiative response:  $(\mathcal{F}_{\uparrow} + \mathcal{F}_{\uparrow}')_{\tau_i}$  at the response level  $p_i$ .  
 828 The bottom boundary condition is that the surface flux equals the (constant) terrestrial black-  
 829 body emission:

$$(\mathcal{F}_{\uparrow})_{\tau_s} = \sigma T_s^4 = (\mathcal{F}_{\uparrow} + \mathcal{F}_{\uparrow}')_{\tau_s + \tau_j'}.$$

830 We distinguish two cases:

- 831 1. If the perturbation level
- $p_j$
- is above the response level
- $p_i$
- , both the transmittivity and
- 
- 832 the atmospheric emission from the surface to the response level are unchanged. Writ-
- 
- 833 ing equation .12 between the surface and response levels shows that the radiative re-
- 
- 834 sponse is unchanged:
- $(\mathcal{F}_{\uparrow}')_{\tau_i + \tau_j'} = 0$
- .
- 
- 835 2. If the perturbation level
- $p_j$
- is below the response level
- $p_i$
- , we first write equation .12
- 
- 836 between the response level and right above the perturbation level:

$$\underbrace{(\mathcal{F}_{\uparrow} + \mathcal{F}_{\uparrow}')_{\tau_i}}_{\text{Flux i}} = \underbrace{e^{-(\tau_j - \tau_i)}}_{\text{Transmittivity i} \rightarrow \text{j}} \left[ \underbrace{(\mathcal{F}_{\uparrow} + \mathcal{F}_{\uparrow}')_{\tau_j}}_{\text{Flux j}} + \underbrace{\sigma \int_{\tau_i}^{\tau_j} T^4 e^{-\tau'} d\tau'}_{\text{Atm emission i} \rightarrow \text{j}} \right], \quad (13)$$

 837 where the temperature profile in optical thickness space  $T(\tau)$  is unperturbed because  
 838 we are above the perturbation level. Subtracting equation .12 to .13 relates the pertur-

839

bation fluxes at levels  $p_i$  and  $p_j$ :

$$\underbrace{\left(\mathcal{F}'_{\uparrow}\right)_{\tau_i}}_{\text{Perturbation flux } i} = \underbrace{e^{-(\tau_j - \tau_i)}}_{\text{Transmittivity } i \rightarrow j} \underbrace{\left(\mathcal{F}'_{\uparrow}\right)_{\tau_j}}_{\text{Perturbation flux } j}. \quad (14)$$

840

841

842

843

Then, we write equation .12 between the surface and right below the perturbation level, use the fact that the temperature profile does not change in pressure space, and use equation .12 between the surface and level  $p_j$  before the perturbation was introduced:

$$\begin{aligned} \underbrace{\left(\mathcal{F}_{\uparrow} + \mathcal{F}'_{\uparrow}\right)_{\tau_j + \tau'_j}}_{\text{Flux below pert}} & \stackrel{\text{Equation .12}}{=} \underbrace{e^{-(\tau_j - \tau_s)}}_{\text{Transmittivity } s \rightarrow j} \left[ \underbrace{\left(\mathcal{F}_{\uparrow} + \mathcal{F}'_{\uparrow}\right)_{\tau_s + \tau'_j}}_{\text{Surface flux}} + \underbrace{\sigma \int_{\tau_j + \tau'_j}^{\tau_s + \tau'_j} (T + T')^4 e^{-\tau'} d\tau'}_{\text{Atm emission } s \rightarrow j} \right] \\ & \stackrel{T(p) = (T + T')(p)}{=} \underbrace{e^{-(\tau_j - \tau_s)}}_{\text{Transmittivity } s \rightarrow j} \left[ \underbrace{\left(\mathcal{F}_{\uparrow}\right)_{\tau_s}}_{\text{Surface flux}} + \underbrace{\sigma \int_{\tau_j}^{\tau_s} T^4 e^{-\tau'} d\tau'}_{\text{Atm emission } s \rightarrow j} \right] \\ & \stackrel{\text{Equation .12}}{=} \underbrace{\left(\mathcal{F}_{\uparrow}\right)_{\tau_j}}_{\text{Flux before pert}}. \end{aligned} \quad (15)$$

844

845

We can now express the perturbation flux at level  $j$  as a function of the total flux at level  $j$  to first order:

$$\begin{aligned} \left(\mathcal{F}'_{\uparrow}\right)_{\tau_j} & \stackrel{\text{First order}}{=} \left(\mathcal{F}'_{\uparrow}\right)_{\tau_j + \tau'_j} \\ & \stackrel{\text{Equation .15}}{=} \left(\mathcal{F}_{\uparrow}\right)_{\tau_j} - \left(\mathcal{F}_{\uparrow}\right)_{\tau_j + \tau'_j} \\ & \stackrel{\text{First order}}{=} - \left(\frac{d\mathcal{F}_{\uparrow}}{d\tau}\right)_{\tau_j} \tau'_j \\ & \stackrel{\text{Equation .11}}{=} \left[\sigma T_j^4 - \left(\mathcal{F}_{\uparrow}\right)_{\tau_j}\right] \tau'_j \\ & \stackrel{\text{Equation 25}}{=} \left[\sigma T_j^4 - \left(\mathcal{F}_{\uparrow}\right)_{\tau_j}\right] \frac{\kappa (f_1 f'_2)_{\tau_j}}{g} \\ & \stackrel{\text{First order}}{=} \frac{\kappa}{g} \left(f_1 \frac{df_2}{dq}\right)_{\tau_j} \left[\sigma T_j^4 - \left(\mathcal{F}_{\uparrow}\right)_{\tau_j}\right] q'_j \\ \left(\mathcal{F}'_{\uparrow}\right)_{\tau_j} & \stackrel{\text{Equation .14}}{=} \frac{\kappa}{g} \left(f_1 \frac{df_2}{dq}\right)_{\tau_j} e^{-|\tau_i - \tau_j|} \left[\sigma T_j^4 - \left(\mathcal{F}_{\uparrow}\right)_{\tau_j}\right] q'_j \end{aligned} \quad (16)$$

846

It is possible to use a similar reasoning for the downwelling flux and find that:

847

848

1. If the perturbation level  $p_j$  is above the response level  $p_i$ , the downwelling flux is perturbed, and to first order:

$$\left(\mathcal{F}'_{\downarrow}\right)_{\tau_i} = \frac{\kappa}{g} \left(f_1 \frac{df_2}{dq}\right)_{\tau_j} e^{-|\tau_i - \tau_j|} \left[\sigma T_j^4 - \left(\mathcal{F}_{\downarrow}\right)_{\tau_j}\right] q'_j. \quad (17)$$

849

850

2. If the perturbation level  $p_j$  is below the response level  $p_i$ , the downwelling flux is unchanged.

851 Combining equations .10, .16 and .17 leads to the longwave linear response (equation 27) by  
852 using its definition:

$$(M_{\text{LW}})_{ij} \stackrel{\text{def}}{=} \frac{g\alpha_i}{L_v q'_j} \left( \frac{d\mathcal{F}_{\text{LW}}'}{dp} \right)_{p_i}. \quad (18)$$

### 853 B.2. One-stream model of shortwave radiation

854 First, we linearize the shortwave flux convergence, given by equation 31, about RCE:

$$-\frac{g}{\kappa} \frac{d\mathcal{F}_{\text{SW}}'}{dp} = \varepsilon f_1 f_2' \mathcal{F}_{\text{SW}} + \varepsilon f_1 f_2 \mathcal{F}'_{\text{SW}}, \quad (19)$$

855 This time, we directly perturb the analytical solution for the downwelling shortwave flux:

$$\frac{\mathcal{F}_{\text{SW}}}{S} = e^{-\varepsilon\tau}, \quad (20)$$

$$\frac{\mathcal{F}'_{\text{SW}}}{S} = e^{-\varepsilon\tau} \left( e^{-\varepsilon\kappa g^{-1} \int_0^p f_1 f_2' - 1} \right). \quad (21)$$

857 Then again, we introduce a water vapor perturbation  $q'_j$  in a thin pressure layer  $[p_j - \Delta p/2, p_j +$   
858  $\Delta p/2]$ , for which  $\Delta p \ll p_j$ , and use the smallness of  $\Delta p/p_j$  to simplify the form of the per-  
859 turbation fluxes at a given level  $p_i$ :

$$\left( \frac{\mathcal{F}'_{\text{SW}}}{S} \right)_{p_i} = e^{-\varepsilon\tau_i} \frac{\varepsilon\kappa\Delta p}{g} (f_1 f_2')_{p_j} \delta_{i < j}. \quad (22)$$

860 Combining equations .19 and .22 leads to the shortwave linear response (equation 32) by  
861 using its definition:

$$(M_{\text{SW}})_{ij} \stackrel{\text{def}}{=} -\frac{g\alpha_i}{L_v q'_j} \left( \frac{d\mathcal{F}'_{\text{SW}}}{dp} \right)_{p_i}. \quad (23)$$

### 862 B.3. Choice of the optical thickness

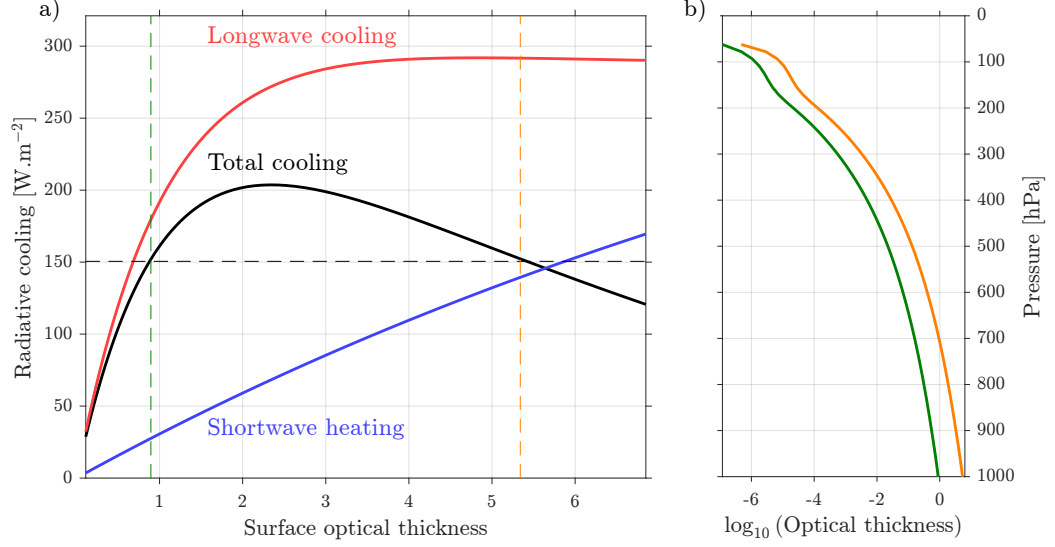
863 For consistency with *Beucler and Cronin* [2016], we represent the optical thickness for  
864 Figure 9 using the following functions of pressure in equations 25 and 30:

$$\kappa = 0.17\text{m}^2 \cdot \text{kg}^{-1}, \quad f_1(p) = \frac{p}{p_s}, \quad f_2(q) = q, \quad \varepsilon(p) \approx 0.077.$$

865 This choice assumes a simple pressure broadening of water vapor, neglects the greenhouse  
866 effects of gas other than water vapor, and estimates the total shortwave absorption using  
867 equation 20 of *Beucler and Cronin* [2016]. The net radiative cooling (sum of equations 17  
868 and 21 in *Beucler and Cronin* [2016]) as a function of the free-tropospheric optical thickness  
869 is depicted in Figure .13, as well as its longwave and shortwave components. The net radi-  
870 ative cooling (black line) matches the radiative cooling computed by RRTM ( $150 \text{ Wm}^{-2}$ ) for  
871 two choices of the absorption coefficient:  $\kappa = (0.022, 0.17) \text{ m}^2 \cdot \text{kg}^{-1}$ , corresponding to two  
872 surface optical thicknesses of (0.8, 5.4). For the gray radiative linear response matrix, we  
873 choose the optically thick solution  $\kappa = 0.17 \text{ m}^2 \cdot \text{kg}^{-1}$  (orange lines), for which the radiative  
874 cooling decreases with surface optical thickness and moisture radiative-cooling instability  
875 can occur [*Beucler and Cronin*, 2016].

## 883 Appendix C: Sensitivity to convective model parameters

884 In this section, we investigate how the stability of the linear response depends on the  
885 convective parameters  $\tau_{\text{BM}}$  and  $\widehat{Q}_{\text{BP}}$ . Following section 5, we combine the Betts-Miller con-



876 **Figure .13.** (a) Free-tropospheric longwave cooling (red line) and shortwave heating (blue line) and total  
 877 net radiative cooling (black line) in  $\text{W}\cdot\text{m}^{-2}$ , versus surface optical thickness. The net radiative cooling in SAM  
 878 is denoted with a dotted black line, and intersects the total radiative cooling of the gray model for two values  
 879 of the surface optical thickness (denoted with green and orange vertical dotted lines). (b) Logarithm 10 of  
 880 optical thickness profile in pressure space when the absorption coefficient is  $\kappa = 0.022\text{m}^2\cdot\text{kg}^{-1}$  (green line)  
 881 and  $\kappa = 0.17\text{m}^2\cdot\text{kg}^{-1}$  (orange line).

886 vective response and the bulk-plume convective response with the real-gas radiative response  
 887 in order to obtain the full linear response and study the linear evolution of small water vapor  
 888 perturbations. The total Betts-Miller response matrix  $M_{\text{BM}+\text{RRTM}}$  and the total bulk-plume  
 889 response matrix  $M_{\text{BP}+\text{RRTM}}$  are given by:

$$M_{\text{BM}+\text{RRTM}}(\tau_{\text{BM}}) = M_{\text{BM}}(\tau_{\text{BM}}) + M_{\text{RRTM}}, \quad (.24)$$

890

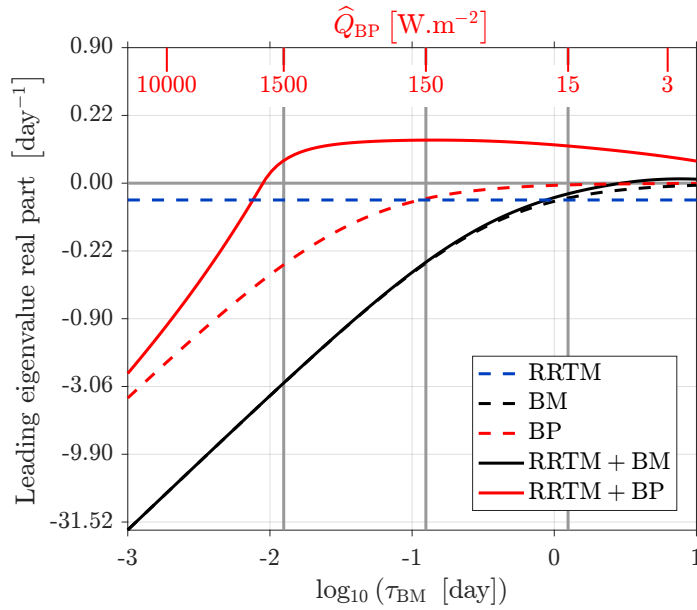
$$M_{\text{BP}+\text{RRTM}}(\widehat{Q}_{\text{BP}}) = M_{\text{BP}}(\widehat{Q}_{\text{BP}}) + M_{\text{RRTM}}, \quad (.25)$$

891 where the Betts-Miller convective response  $M_{\text{BM}}$  depends on the Betts-Miller timescale  $\tau_{\text{BM}}$   
 892 and the bulk-plume convective response  $M_{\text{BP}}$  depends on the radiative cooling parameter  
 893  $\widehat{Q}_{\text{BP}}$ , while the radiative response  $M_{\text{RRTM}}$  remains unchanged for a fixed surface tempera-  
 894 ture.

900 In figure .14, we define the range of realistic convective parameters as  $\tau_{\text{BM}}$  between 0.3  
 901 and 30 hours, and  $\widehat{Q}_{\text{BP}} = 150$  between 15 and  $1500 \text{ W}\cdot\text{m}^{-2}$ . Over this wide range of convec-  
 902 tive parameters, none of the leading eigenvalue real parts change sign. The combined RRTM  
 903 and bulk-plume response is the only linearly unstable response with an average growth rate of  
 904 10.0 days over the realistic range of parameters.

### 905 Acknowledgments

906 We thank Zhiming Kuang for providing the data described in section 3.1.1, Tristan Abbott  
 907 for providing the data described in section 3.1.2, Adam Sobel and an anonymous reviewer  
 908 for writing thoughtful and constructive reviews of the present manuscript. Tom Beucler  
 909 thanks Rohini Shivamoggi for helpful suggestions that improved the clarity of the present  
 910 manuscript. He also thanks Daniel Gilford and Marianna Linz for their help with the mi-



895 **Figure .14.** Leading eigenvalue real part of the 300K linear response (in  $\text{day}^{-1}$ ) as a function of  
 896  $\log_{10} \tau_{\text{BM}}$  (in hours, for the RRTM+BM and BM cases) and  $\widehat{Q}_{\text{BP}}$  (in  $\text{W m}^{-2}$ , for the RRTM+BP and BP  
 897 cases). The scale for  $\tau_{\text{BM}}$  and the scale for  $\widehat{Q}_{\text{BP}}$  are aligned so that the responses depicted on figure 5 (BM,  
 898  $\tau_{\text{BM}} = 3$  hours) and 7 (BP,  $\widehat{Q}_{\text{BP}} = 150 \text{ W m}^{-2}$ ) fall on the same vertical line (central vertical gray line). The  
 899 two other vertical gray lines indicate the range of realistic convective parameters.

911 crophysics and statistical analysis tools that were used to analyze the results from the MIT  
 912 Single Column Model (presented in the supplementary material). He was supported under  
 913 NSF grants AGS-1136480 and AGS-1418508. Timothy W. Cronin was supported by NSF  
 914 grant AGS-1623218. The source code and data used to produce the Figures can be found at  
 915 [https://github.com/tbeucler/Linear\\_response\\_framework\\_RCI](https://github.com/tbeucler/Linear_response_framework_RCI), except for Figure  
 916 3's data which was provided by Z. Kuang.

## 917 References

- 918 Adames, A.F. and D. Kim, 2016: The MJO as a Dispersive, Convectively Coupled Moisture  
 919 Wave: Theory and Observations, *Journal of the Atmospheric Sciences*, 73, 913-941,  
 920 doi:10.1175/JAS-D-15-0170.1.
- 921 Arakawa, A., and W. H. Schubert (1974), Interaction of a Cumulus Cloud Ensemble with the  
 922 Large-Scale Environment, Part I, doi:10.1175/1520-0469(1974)031<0674:IOACCE>2.0.  
 923 CO;2.
- 924 Betts, A. K., and M. J. Miller (1986), A new convective adjustment scheme. Part II: Single  
 925 column tests using GATE wave, BOMEX, ATEX and arctic air-mass data sets, *Quar-*  
 926 *terly Journal of the Royal Meteorological Society*, 112(473), 693-709, doi:10.1002/qj.  
 927 49711247308.
- 928 Betts, A. K., and M. J. Miller (1993), *The Betts-Miller Scheme*, pp. 107-121, American Me-  
 929 *teorological Society*, Boston, MA, doi:10.1007/978-1-935704-13-3\_9.
- 930 Beucler, T., and T. W. Cronin (2016), Moisture-radiative cooling instability, *Journal of Ad-*  
 931 *vances in Modeling Earth Systems* doi:10.1002/2016MS000763.
- 932 Bjerknes (1938), Saturated-adiabatic ascent of air, (2), 325-330.
- 933 Bolton, D. (1980), The Computation of Equivalent Potential Temperature, *Monthly Weather*  
 934 *Review*, 108(7), 1046-1053, doi:10.1175/1520-0493(1980)108<1046:TCOEPT>2.0.CO;  
 935 2.

- 936 Bony, S., B. Stevens, D. Coppin, T. Becker, K. A. Reed, A. Voigt, and B. Medeiros (2016),  
 937 Thermodynamic control of anvil cloud amount, *Proceedings of the National Academy of*  
 938 *Sciences*, 113(32), 8927–8932, doi:10.1073/pnas.1601472113.
- 939 Bretherton, C. S., P. N. Blossey, and M. Khairoutdinov (2005), An Energy-Balance Analysis  
 940 of Deep Convective Self-Aggregation above Uniform SST, *Journal of the Atmospheric*  
 941 *Sciences*, 62(12), 4273–4292, doi:10.1175/JAS3614.1.
- 942 Chikira, M. (2014), Eastward-Propagating Intraseasonal Oscillation Represented by Chikira  
 943 Sugiyama Cumulus Parameterization. Part II: Understanding Moisture Variation under  
 944 Weak Temperature Gradient Balance, *Journal of the Atmospheric Sciences*, 71(2), 615–  
 945 639, doi:10.1175/JAS-D-13-038.1.
- 946 Ciesielski, P. E., R. H. Johnson, P. T. Haertel, and J. Wang (2003), Corrected TOGA COARE  
 947 sounding humidity data: Impact on diagnosed properties of convection and climate over  
 948 the warm pool, *Journal of Climate*, 16(14), 2370–2384, doi:10.1175/2790.1.
- 949 Collins, W.D., C.M. Bitz, M.L. Blackmon, G.B. Bonan, C.S. Bretherton, J.A. Carton, P.  
 950 Chang, S.C. Doney, J.J. Hack, T.B. Henderson, J.T. Kiehl, W.G. Large, D.S. McKenna,  
 951 B.D. Santer, and R.D. Smith, 2006, The Community Climate System Model Version 3  
 952 (CCSM3), *Journal of Climate*, 19, 2122–2143, doi:10.1175/JCLI3761.1
- 953 Coppin, D., and S. Bony (2017), Internal variability in a coupled General Circulation  
 954 Model in Radiative-Convective Equilibrium, *Geophysical Research Letters*, doi:10.1002/  
 955 2017GL073658.
- 956 Dee, D. P., S. M. Uppala, A. J. Simmons, P. Berrisford, P. Poli, S. Kobayashi, U. Andrae,  
 957 M. A. Balsameda, G. Balsamo, P. Bauer, P. Bechtold, A. C. M. Beljaars, L. van de Berg,  
 958 J. Bidlot, N. Bormann, C. Delsol, R. Dragani, M. Fuentes, A. J. Geer, L. Haimberger,  
 959 S. B. Healy, H. Hersbach, E. V. Holm, L. Isaksen, P. Kollberg, M. Kohler, M. Matricardi,  
 960 A. P. McNally, B. M. Monge-Sanz, J. J. Morcrette, B. K. Park, C. Peubey, P. de Rosnay,  
 961 C. Tavolato, J. N. Thopaut, and F. Vitart (2011), The ERA-Interim reanalysis: Configu-  
 962 ration and performance of the data assimilation system, *Quarterly Journal of the Royal*  
 963 *Meteorological Society*, 137(656), 553–597, doi:10.1002/qj.828.
- 964 Emanuel, K. a. (1991), A Scheme for Representing Cumulus Convection in Large-Scale  
 965 Models, doi:10.1175/1520-0469(1991)048<2313:ASFRCC>2.0.CO;2.
- 966 Emanuel, K. A. (1994), *Atmospheric convection*, 1–580 pp., Oxford University Press.
- 967 Emanuel, K. A., and M. Živković-Rothman (1999), Development and Evaluation of a Con-  
 968 vection Scheme for Use in Climate Models, *Journal of the Atmospheric Sciences*, 56(11),  
 969 1766–1782, doi:10.1175/1520-0469(1999)056<1766:DAEOAC>2.0.CO;2.
- 970 Emanuel, K. a., A. a. Wing, and E. M. Vincent (2014), Radiative-convective instability,  
 971 *Journal of Advances in Modeling Earth Systems*, 5(November), n/a–n/a, doi:10.1002/  
 972 2013MS000270.
- 973 Fouquart, Y., and B. Bonnel (1980), Computations of solar heating of the earth’s  
 974 atmosphere- A new parameterization, *Beitraege zur Physik der Atmosphaere*, 53, 35–62.
- 975 Frierson, D. M. W. (2007), The Dynamics of Idealized Convection Schemes and Their Effect  
 976 on the Zonally Averaged Tropical Circulation, *Journal of the Atmospheric Sciences*, 64(6),  
 977 1959–1976, doi:10.1175/JAS3935.1.
- 978 Grabowski, W. W., and M. W. Moncrieff (2004), Moisture-convection feedback in the trop-  
 979 ics, *Quarterly Journal of the Royal Meteorological Society*, 130(604), 3081–3104, doi:  
 980 10.1256/qj.03.135.
- 981 Hannah, W. M., and E. D. Maloney (2011), The role of moisture-convection feedbacks in  
 982 simulating the Madden-Julian oscillation, *Journal of Climate*, 24(11), 2754–2770, doi:  
 983 10.1175/2011JCLI3803.1.
- 984 Hartman, P. (1960), A lemma in the theory of structural stability of differential equa-  
 985 tions, *Proceedings of the American Mathematical Society*, 11(4), 610–610, doi:10.1090/  
 986 S0002-9939-1960-0121542-7.
- 987 Hartmann, D. L., and K. Larson (2002), An important constraint on tropical cloud - climate  
 988 feedback, *Geophysical Research Letters*, 29(20), 12–1–12–4, doi:10.1029/2002GL015835.

- 989 Hastings, W. K. (1970), Monte carlo sampling methods using Markov chains and their appli-  
990 cations, *Biometrika*, 57(1), 97–109, doi:10.1093/biomet/57.1.97.
- 991 Herman, M. J., and Z. Kuang (2013), Linear response functions of two convective parame-  
992 terization schemes, *Journal of Advances in Modeling Earth Systems*, 5(3), 510–541, doi:  
993 10.1002/jame.20037.
- 994 Holloway, C. E., and J. D. Neelin (2009), Moisture Vertical Structure, Column Water Vapor,  
995 and Tropical Deep Convection, *Journal of the Atmospheric Sciences*, 66(6), 1665–1683,  
996 doi:10.1175/2008JAS2806.1.
- 997 Holloway, C. E., and S. J. Woolnough (2016), The sensitivity of convective aggregation to  
998 diabatic processes in idealized radiative-convective equilibrium simulations, *Journal of*  
999 *Advances in Modeling Earth Systems*, 8(1), 166–195, doi:10.1002/2015MS000511.
- 1000 Iacono, M. J., E. J. Mlawer, S. A. Clough, and J.-J. Morcrette (2000), Impact of an improved  
1001 longwave radiation model, RRTM, on the energy budget and thermodynamic properties of  
1002 the NCAR community climate model, CCM3, *Journal of Geophysical Research: Atmo-*  
1003 *spheres*, 105(D11), 14,873–14,890, doi:10.1029/2000JD900091.
- 1004 Iacono, M. J., J. S. Delamere, E. J. Mlawer, M. W. Shephard, S. A. Clough, and W. D.  
1005 Collins (2008), Radiative forcing by long-lived greenhouse gases: Calculations with  
1006 the AER radia- tive transfer models, *Journal of Geophysical Research Atmospheres*,  
1007 113(D13103), doi:10.1029/2008jd009944.
- 1008 Inoue, K., and L. Back (2015), Column-Integrated Moist Static Energy Budget Analysis on  
1009 Various Time Scales during TOGA COARE, *Journal of the Atmospheric Sciences*, 72(5),  
1010 1856–1871, doi:10.1175/JAS-D-14-0249.1.
- 1011 , Khairoutdinov, M.F. and D.A. Randall, 2003, Cloud Resolving Modeling of the ARM  
1012 Summer 1997 IOP: Model Formulation, Results, Uncertainties, and Sensitivities, *Jour-*  
1013 *nal of the Atmospheric Sciences*, 60, 607–625, doi:10.1175/1520-0469(2003)060<0607:  
1014 CRMOTA>2.0.CO;2.
- 1015 Kuang, Z. (2010), Linear Response Functions of a Cumulus Ensemble to Temperature and  
1016 Moisture Perturbations and Implications for the Dynamics of Convectively Coupled  
1017 Waves, *Journal of the Atmospheric Sciences*, 67(4), 941–962, doi:10.1175/2009JAS3260.  
1018 1.
- 1019 Kuang, Z. (2012), Weakly Forced Mock Walker Cells, *Journal of the Atmospheric Sciences*,  
1020 69(9), 2759–2786, doi:10.1175/JAS-D-11-0307.1.
- 1021 Malkus, J. S., C. Ronne, and M. Chafee (1961), Cloud Patterns in Hurricane Daisy, 1958,  
1022 *Tellus*, 13(1), 8–30, doi:10.1111/j.2153-3490.1961.tb00062.x.
- 1023 Mapes, B., and R. Neale (2011), Parameterizing convective organization to escape the en-  
1024 trainment dilemma, *Journal of Advances in Modeling Earth Systems*, 3(2), n/a–n/a, doi:  
1025 10.1029/2011MS000042.
- 1026 Metropolis, N., A. W. Rosenbluth, M. N. Rosenbluth, A. H. Teller, and E. Teller (1953),  
1027 Equation of State by Fast Computing Machines, *The Journal of Chemical Physics*,  
1028 21(1953), 1087–1092, doi:10.1063/1.1699114.
- 1029 Mlawer, E. J., S. J. Taubman, P. D. Brown, M. J. Iacono, and S. A. Clough (1997), Radiative  
1030 transfer for inhomogeneous atmospheres: RRTM, a validated correlated-k model for the  
1031 longwave, *Journal of Geophysical Research: Atmospheres*, 102(D14), 16,663–16,682,  
1032 doi:10.1029/97JD00237.
- 1033 Morcrette, J.-J. (1991), Radiation and cloud radiative properties in the European Centre for  
1034 Medium Range Weather Forecasts forecasting system, *Journal of Geophysical Research*,  
1035 96(D5), 9121, doi:10.1029/89JD01597.
- 1036 Muller, C., and S. Bony (2015), What favors convective aggregation and why ?, pp. 5626–  
1037 5634, doi:10.1002/2015GL064260.Received.
- 1038 Muller, C. J., and I. M. Held (2012), Detailed Investigation of the Self-Aggregation of Con-  
1039 vection in Cloud-Resolving Simulations, *Journal of the Atmospheric Sciences*, 69, 2551–  
1040 2565, doi:10.1175/JAS-D-11-0257.1.
- 1041 Pauluis, O. M., and A. A. Mrowiec (2013), Isentropic Analysis of Convective Motions, *Jour-*  
1042 *nal of the Atmospheric Sciences*, 70(11), 3673–3688, doi:10.1175/JAS-D-12-0205.1.

- 1043 Pierrehumbert, R. T. (2009), Principles of Planetary Climate, *Earth*, 1, 359.
- 1044 Plant, R. S. (2009), A review of the theoretical basis for bulk mass flux convective pa-  
1045 rameterization, *Atmospheric Chemistry and Physics*, pp. 3529–3544, doi:10.5194/  
1046 acpd-9-24945-2009.
- 1047 Ramanathan, V., and J. A. Coakley (1978), Climate modeling through radiative-convective  
1048 models, *Reviews of Geophysics*, 16(4), 465–489, doi:10.1029/RG016i004p00465.
- 1049 Renno, N. O., P. H. Stone, and K. A. Emanuel (1994), Radiative-convective model with an  
1050 explicit hydrologic cycle. 2: Sensitivity to large changes in solar forcing, doi:10.1029/  
1051 94JD01332.
- 1052 Romps, D. M. (2014), An analytical model for tropical relative humidity, *Journal of Climate*,  
1053 27(19), 7432–7449, doi:10.1175/JCLI-D-14-00255.1.
- 1054 Sengupta, D., B. N. Goswami, and R. Senan (2001), Coherent intraseasonal oscillations of  
1055 ocean and atmosphere during the Asian summer monsoon, *Geophysical Research Letters*,  
1056 28(21), 4127–4130, doi:10.1029/2001GL013587.
- 1057 Sherwood, S. C., W. Ingram, Y. Tsushima, M. Satoh, M. Roberts, P. L. Vidale, and P. A.  
1058 O’Gorman (2010), Relative humidity changes in a warmer climate, *Journal of Geophys-  
1059 ical Research Atmospheres*, 115(9), D09,104, doi:10.1029/2009JD012585.
- 1060 Singh, M. S., and P. A. O’Gorman (2013), Influence of entrainment on the thermal stratifi-  
1061 cation in simulations of radiative-convective equilibrium, *Geophysical Research Letters*,  
1062 40(16), 4398–4403, doi:10.1002/grl.50796.
- 1063 Sobel, A.H. and C.S. Bretherton, 2000: Modeling Tropical Precipitation in a Single Col-  
1064 umn, *Journal of Climate*, 13, 4378–4392, doi:10.1175/1520-0442(2000)013<4378:  
1065 MTPIAS>2.0.CO;2.
- 1066 Sobel, A.H. and H. Gildor, 2003: A Simple Time-Dependent Model of SST Hot  
1067 Spots, *Journal of Climate*, 16, 3978–3992, doi:10.1175/1520-0442(2003)016<3978:  
1068 ASTMOS>2.0.CO;2.
- 1069 Sobel, A. H., J. Nilsson, and L. M. Polvani (2001), The Weak Temperature Gradient Approx-  
1070 imation and Balanced Tropical Moisture Waves, *Journal of the Atmospheric Sciences*, 58,  
1071 3650–3665, doi:10.1175/1520-0469(2001)058<3650:TWTGAA>2.0.CO;2.
- 1072 . Stansifer, E. M., O’Gorman, P. A., & Holt, J. I. (2017), Accurate computation of moist  
1073 available potential energy with the Munkres algorithm. *Quarterly Journal of the Royal  
1074 Meteorological Society*, 143(702), 2887–2922. doi:10.1002/qj.2921.
- 1075 Tompkins, A. M. (2001), Organization of Tropical Convection in Low Vertical Wind Shears:  
1076 The Role of Cold Pools, *Journal of the Atmospheric Sciences*, 58, 1650–1672, doi:  
1077 10.1175/1520-0469(2001)058<1650:OOTCIL>2.0.CO;2.
- 1078 Tompkins, AM; Semie, AG (2017), *Organization of tropical convection in low vertical wind  
1079 shears: role of updraft entrainment*, *Journal of Advances in Modeling Earth Systems*, doi:  
1080 10.1002/2016MS000802.
- 1081 Vecchi, G. A., and D. E. Harrison (2002), Monsoon breaks and subseasonal sea surface tem-  
1082 perature variability in the Bay of Bengal, *Journal of Climate*, 15(12), 1485–1493, doi:  
1083 10.1175/1520-0442(2002)015<1485:MBASSS>2.0.CO;2.
- 1084 Wing, A. A., and T. W. Cronin (2016), Self-aggregation of convection in long channel ge-  
1085 ometry, *Quarterly Journal of the Royal Meteorological Society*, 142(694), 1–15, doi:  
1086 10.1002/qj.2628.
- 1087 Wing, A. a., and K. a. Emanuel (2014), Physical mechanisms controlling self-aggregation of  
1088 convection in idealized numerical modeling simulations, *Journal of Advances in Modeling  
1089 Earth Systems*, 5(November), 59–74, doi:10.1002/2013MS000269.
- 1090 Wing, A. A., S. J. Camargo, and A. H. Sobel (2016), Role of radiative-convective feedbacks  
1091 in spontaneous tropical cyclogenesis in idealized numerical simulations, *Journal of the  
1092 Atmospheric Sciences*, 73(7), JAS–D–15–0380.1, doi:10.1175/JAS-D-15-0380.1.
- 1093 Wing, A. A., K. Emanuel, C. E. Holloway, and C. Muller (2017), Convective Self-  
1094 Aggregation in Numerical Simulations: A Review, *Surveys in Geophysics*, doi:10.1007/  
1095 s10712-017-9408-4.

- 1096 Wolding, B. O., E. D. Maloney, S. Henderson, and M. Branson (2016), Climate Change and  
1097 the Madden-Julian Oscillation : A Vertically Resolved Weak Temperature Gradient Analy-  
1098 sis, *Journal of Advances in Modeling Earth Systems*, doi:10.1002/2016MS000843.
- 1099 Yanai, M., S. Esbensen, and J.-H. Chu (1973), Determination of Bulk Properties of  
1100 Tropical Cloud Clusters from Large-Scale Heat and Moisture Budgets, doi:10.1175/  
1101 1520-0469(1973)030<0611:DOBPOT>2.0.CO;2.
- 1102 Yu, J.-Y., C. Chou, and J. D. Neelin (1998), Estimating the Gross Moist Stability of the  
1103 Tropical Atmosphere\*, *Journal of the Atmospheric Sciences*, 55(8), 1354–1372, doi:  
1104 10.1175/1520-0469(1998)055<1354:ETGMSO>2.0.CO;2.